Large eddy simulation of a utility-scale horizontal axis turbine with woody debris accumulation under live bed conditions

Mustafa Meriç Aksen[a], Hossein Seyedzadeh[a], Mehrshad Gholami Anjiraki[a], Jonathan Craig[a], Kevin Flora[a], Christian Santoni[a], Fotis Sotiropoulos[b], and Ali Khosronejad[a*]

[a] Department of Civil Engineering, Stony Brook University, Stony Brook, NY 11794, USA
[b] Mechanical and Nuclear Engineering, Virginia Commonwealth University, Richmond, VA 23284, USA

Large eddy simulation of a utility-scale horizontal axis turbine with woody debris accumulation under live bed conditions

Mustafa Meriç Aksen[a], Hossein Seyedzadeh[a], Mehrshad Gholami Anjiraki[a], Jonathan Craig[a], Kevin Flora[a], Christian Santoni[a], Fotis Sotiropoulos[b], Ali Khosronejad[a,*]

[a]*Department of Civil Engineering, Stony Brook University, Stony Brook, NY 11794, USA*
[b] *Mechanical and Nuclear Engineering, Virginia Commonwealth University, Richmond, VA 23284, USA*

Abstract

Tidal and riverine flows are viable energy sources for consistent energy production. Installing and operating marine hydrokinetic (MHK) turbines requires assessing any potential impact of debris accumulation on turbine performance and sediment transport. More specifically, MHK devices may alter the natural sediment transport processes and cause debris accumulation, disrupting the natural sediment dynamic. In turn, these processes could affect the turbine's performance. We carried out a series of large-eddy simulations coupled with bed morphodynamics, introducing various debris loads lodged on the upstream face of a utility-scale turbine tower. The objective is to systematically investigate the impact of debris accumulation on the performance and hydro- and morpho-dynamics interactions of the horizontal-axis MHK turbine under rigid and mobile bed conditions. To that end, we (1) employed the actuator line and surface methods for modeling turbine blades and the nacelle, respectively, (2) directly resolved individual logs, and (3) solved the Exner equation to obtain the instantaneous bed deformation of the mobile bed. Our analysis revealed that while the spinning rotor amplifies scour around the pile, debris accumulation modifies the sediment dynamics of the system. Also, it found that morphodynamic processes accelerate the wake recovery, slightly enhancing the turbine's performance.

Keywords: Large-eddy simulation, Marine hydrokinetic turbine, Sediment transport, Actuator model, Debris accumulation

1. Introduction

Between 1998 and 2021, renewable energy has grown from 2% to 30% of the global energy demand, and hydropower has constituted a substantial part of the mainstream renewable energies, including wind, solar, and biomass [1–3]. Of this growing percentage of renewable energy, marine renewable energy has been an underused but promising resource. In 2021, the National Renewable Energy Laboratory estimated that marine energy is capable of contributing 2 300 TWh/yr to the United States, approximately 28% of the global energy demand in 2021 [3, 4]. Of the estimated

*Corresponding author
Email address: (Ali Khosronejad).

2 300 TWh/yr, tidal and river energies respectively comprise 220 and 99 TWh/yr, equal to 9.5% and 4.3%, respectively. Most importantly, tidal and riverine flows are viable energy sources due to their high predictability, consistent energy production, and potential array optimization to maximize energy extraction at various sites [4–6]. On the other hand, previous environmental studies have warned that manmade structures might interfere with marine and riverine sediment transport processes, and interactions with floating debris might harmfully impact the flow as well as turbine performance [7–14].

The advancing testing technology has aided research groups at various marine sites in North America and Europe to improve the design and performance of marine hydrokinetic (MHK) turbines [15–19]. Even in light of such diverse and extensive testing, such turbine sites have not reached the commercial stage due to a continued lack of understanding about MHK turbines' environmental effects, which include natural sediment transport processes and floating debris [4, 6, 15, 20–22]. Generally, previous studies have either ignored the complex morphodynamic processes or only considered sediment dynamics in laboratory-scale scenarios. For instance, when Chawdhary et al. [23] performed a high-fidelity simulation of an array of MHK turbines in the East River in New York City, the site's rigid bed obviated the need for modeling sediment transport.

As most marine sites exhibit complex morphodynamics, many experimental studies expanded their scope to include turbine performance and meandering channels [24, 25]. In particular, Musa et al. [26] researched the influence of sand waves on the stability and operation of MHK turbine arrays. Experimental studies have helped the understanding of MHK turbine-sediment interactions, and they serve as a benchmark for computational studies (for further reading, see [24, 27–29]). Nonetheless, difficulties in scaling turbulent flow parameters, including Reynolds number, and the diversity of marine environments limit the testing capability of laboratory flumes [26, 30–34].

Hence, it is imperative to incorporate sediment transport modeling into MHK simulations to achieve comprehensive computational fluid dynamics (CFD) analyses [35–37]. First, Yang et al. [35] studied the sediment-MHK interactions, revealing that higher tip speed ratios (TSR) contribute to increased scour and deposition. They observed faster wake recovery due to bed-induced flow motion, resulting in higher mean kinetic energy. Ramirez-Mendoza et al. [36] employed a combination of experimental and numerical modeling to study wake asymmetries caused by interaction between a hydrokinetic turbine and sediment transport. Finally, Deng et al. [37] investigated the combined effects of existing mono-pile foundations and rotating blades on scour processes, noting increased scour under clear water conditions.

Furthermore, large woody debris (LWD), defined as logs exceeding 1 m in length and 0.147 m in diameter [38], may be transported downstream along the thalweg and may deposit in both alluvial environments (e.g., the floodplains, banks, or channel bed) and on man-made structures [39, 40]. LWDs naturally form heterogeneous clusters when they accumulate on artificial structures, and thus, heterogeneous flow patterns occur with complex turbulence structures, which may cause local scour patterns [41]. Hydro- and morpho-dynamic processes due to the debris accumulation vary significantly depending on the accumulation characteristics such as compactness, accumulation length, permeability, etc. [42, 43].

In a real-life environment, the individual woody logs arbitrary cluster at man-made structures in the computational domain. Even significant aspects of debris accumulation are inherently random, including the previously listed accumulation characteristics. The given uncertainties of debris accumulation complicate turbulent flow around natural debris buildups [44]. For instance, Schalko et al. [45] conducted a study on flow and wake characteristics through laboratory tests, introducing parameters such as submerged or emergent logs and individual logs' positions. They concluded that emergent logs lead to the formation of a von-Karman vortex street (VS), while submerged logs cause a greater velocity deficit and lag in the wake recovery. These LWD-sediment interactions can be adapted for river management purposes, such as river declogging [46] or ecosystem maintenance [47]. Yet, the intricate interplay of flow, sediment transport, and debris accumulating at structures such as bridges or retention racks can lead to destructive consequences, including extreme scouring, backwater rise, and structural damage [48, 49]. Jeon et al. [30] studied the accumulation of floating debris on the laboratory-scale models of bridge foundations, revealing the significant impact of woody debris on the flow field and sediment transport past the bridge foundations, which may resemble feathering turbine behavior.

Given the dynamic nature of bed behavior and debris in natural flow environments, it is imperative to assess the potential impact of debris accumulation on sediment transport and turbine performance in the installation and operation of MHK turbines. Aksen et al. [50] systematically analyzed the performance of MHK turbines by incorporating various debris accumulation configurations, revealing that debris build-up lodged on the turbine tower hinders the flow passing through the MHK turbine at lower depths, consequently reducing efficiency. Importantly, the scope of their study was limited as they considered a flume with a rigid bed in their numerical tests.

According to the authors' knowledge, the current state-of-the-art lacks a comprehensive study to address the interaction of MHK turbines, woody debris, and sediment dynamics. More specifically, the effects of coupled sediment transport and debris buildup on a single utility-scale MHK turbine have not been investigated. Even in a laboratory setting, experimental conditions can not replicate the arbitrarily complex and diverse configurations of debris patterns and morphodynamics [30]. Therefore, in an attempt to address this knowledge gap, we carried out a systematic numerical study to investigate the complex interaction of turbulent flow, turbine, woody logs, and sediment on a utility-scale turbine under both rigid and mobile bed conditions, and explore variations in the flow field, bed morphology, and power production.

The present numerical study investigates the debris impact on a utility-scale MHK turbine performance by considering the following procedures for modeling various aspects of the flow, woody debris cluster, sediment dynamics, and MHK turbine interaction problem: (1) large-eddy simulation (LES) is employed to resolve the turbulent flow field while the flow near solid surfaces is determined using a wall-modeling approach; (2) actuator line model in tandem with the nacelle model resolved using the actuator surface model, denoted as ALN in this study, are utilized to numerically parameterize the MHK turbine's blades and nacelle; (3) a geometry-resolving method is used to capture the effect of accumulated debris on the flow and turbine tower; (4) the Exner-Polya sediment mass-balance equation is utilized to compute the mobile bed's instantaneous deformation, capturing the evolving features of the mobile bed such as bedforms. Given the importance of the interactions among the flow, woody debris accumulation, and the mobile bed's features on the efficiency and operation of MHK turbines, the present study can shed light on some of the unknown dynamics of the axial flow turbines at full scale.

Generally, LES is a more computationally costly approach than engineering models, such as the Reynolds-Averaged Navier Stokes (RANS) model. However, LES could more accurately estimate the instantaneous effects of wake-turbine interactions, bathymetry, and background turbulence [31, 32, 51, 52]. The recent advancements in high-performance computing (HPC), wall-modeling techniques, and the immersed boundary method have enabled us to carry out the LES of the utility-scale MHK turbine. Nonetheless, LES simulation with a turbine-resolving approach entails a high computational cost. To alleviate the additive computational cost, the actuator methods provide a balance between a simplified parameterization of the turbine model and fidelity of results [33, 53]. The three actuator methods are the actuator line (AL), actuator disk (AD), and actuator surface (AS).

Sørensen and Shen [54] first proposed the AL method as an aerodynamic model to include a radial distribution of blade forces and, hence, rotational effects. AD simulations lack rotational effects such as tip-vortex helix instability in the near wake due to the modeling of the turbine blades as a stationary disk [51]. Rotation is a significant feature of 3D turbulent flow as Kang et al. [32] showed that LES-AL agrees better with the turbine-resolved LES than LES-AD, especially with respect to the swirl-velocity profiles in the near wake. Even so, the actuator line method does not incorporate the nacelle in the turbine geometry, which is known to have an impact on certain turbine wake characteristics, such as velocity in the near wake [32, 55–58]. The AS method achieves a higher level of fidelity; however, the insignificant differences in wake flow, power production, and turbulent kinetic energy do not always justify the higher computational cost [58, 59]. As HPC resources have become more accessible, AL has become a common technique for numerical simulations involving wind [60, 61] and hydrokinetic [32, 33, 53, 62] turbines. Therefore, we employed the ALN approach herein.

The subsequent sections are organized as follows. Section 2 contains the governing equations for the hydrodynamic model, the morpho-dynamic model, and the actuator line model. Next, Section 3 describes the setup for the test cases, including the debris configurations and details about the sediment transport model. Section 4 presents and discusses the results of the test cases. Lastly, Section 5 reviews the significance of the findings and their implications for future research.

2. Governing equations

2.1. The hydrodynamic model

In this study, we employ our in-house model, the Virtual Flow Simulator (VFS-Geophysics) code, which solves the time-averaged and spatially-filtered incompressible Navier-Stokes equations within a non-orthogonal, generalized curvilinear coordinate system using the RANS and LES models, respectively. The Navier-Stokes equations transform from Cartesian to curvilinear coordinates by application of the Jacobian of geometric transformation, $J = \left|\partial\left(\xi^1, \xi^2, \xi^3\right)/\partial\left(x_1, x_2, x_3\right)\right|$. The transformed Navier-Stokes equations in compact tensor notation are expressed as such [63]:

$$J\frac{\partial U^j}{\partial \xi^j} = 0 \tag{1}$$

$$\frac{\partial U^i}{\partial t} = \frac{\xi^i_l}{J}\left(\frac{\partial}{\partial \xi^j}\left(U^j u_i\right) + \frac{1}{\rho}\frac{\partial}{\partial \xi^j}\left(\mu\frac{g^{jk}}{J}\frac{\partial u_i}{\partial \xi^k}\right) - \frac{1}{\rho}\frac{\partial}{\partial \xi^j}\left(\frac{\xi^j_i p}{J}\right) - \frac{1}{\rho}\frac{\partial \tau_{ij}}{\partial \xi^j} + F_{\text{ext}}\right) \tag{2}$$

where u_i represents the i-th filtered velocity component in Cartesian coordinates. The contravariant volume flux is defined as $U^i = \left(\xi^i_m/J\right) u_m$, where $\xi^i_l = \partial\xi^i/\partial x_l$ is the transformation matrix. The components of the contravariant metric tensor are denoted as $g^{jk} = \xi^j_l\, \xi^k_l$. p represents the pressure, μ represents the fluid's dynamic viscosity, and ρ represents the fluid's density. The drag and lift forces behave as external forces (denoted as F_{ext} in Eq.(2)) per unit volume, serving as a source term for the momentum. τ_{ij} is the Reynolds stress tensor, which is unknown. This study closes the Navier-Stokes equations with LES and RANS models to resolve τ_{ij}.

In the LES approach, sub-grid stress terms arise in the filtered Navier-Stokes equations (Eq.(1) and Eq.(2)), which are approximated by the Smagorinsky sub-grid scale (SGS) model [64–66]:

$$\tau_{ij} = -2\mu_{\text{t}}\overline{S_{ij}} + \frac{1}{3}\tau_{kk}\delta_{ij} \tag{3}$$

$$\mu_{\text{t}} = C_{\text{s}}\Delta^2\left|\overline{S}\right| \tag{4}$$

where μ_{t} represents the eddy viscosity, the overbar denotes the grid filtering operation, $\overline{S_{ij}}$ is the filtered strain-rate tensor, C_{s} denotes the Smagorinsky constant, δ_{ij} denotes the Kronecker delta, and Δ is the filter size.

In the RANS model, τ_{ij} is approximated by the Boussinesq hypothesis:

$$\tau_{ij} = -2\mu_t \tilde{S}_{ij} + \frac{2}{3}\rho k \delta_{ij} \tag{5}$$

where $\tilde{S}_{ij}$ signifies the Reynolds-averaged strain-rate tensor, and k represents the turbulence kinetic energy. To close the RANS equations, the $k-\omega$ model [67] is utilized. The generalized curvilinear system of $k-\omega$ model is written as follows [64]:

$$\frac{1}{J}\frac{\partial(\rho k)}{\partial t} + \frac{\partial}{\partial \xi_j}\left(\rho k U_j\right) = \tau_{ij}\frac{\xi_j^k}{J}\frac{\partial u_i}{\partial \xi_k} - \frac{1}{J}\beta^* \rho k \omega \tag{6}$$

$$\frac{1}{J}\frac{\partial(\rho \omega)}{\partial t} + \frac{\partial}{\partial \xi_j}\left(\rho \omega U_j\right) = \alpha\frac{\rho\omega}{k}\tau_{ij}\frac{\xi_j^k}{J}\frac{\partial u_i}{\partial \xi_k} - \frac{1}{J}\beta \rho \omega^2 \tag{7}$$

where k is the turbulence kinetic energy, ω is the specific rate of dissipation of the turbulence kinetic energy into internal thermal energy, $\alpha = 5/9$, $\beta = 3/40$, $\beta^* = 9/100$, and $\sigma^* = 1/2$ represent the coefficients of closure. μ_t represents the dynamic eddy viscosity (=$\rho k/\omega$).

2.2. The morphodynamic model

This study considers only the bedload sediment transport within the bedload (or saltation) layer. The bedload layer is a live layer of thickness, δ_{BL}, which is set equal to three times the median grain size of the sediment particles ($3d_{50}$). The continuity equation for sediment, also known as the Exner-Polya equation, is therefore solved within the saltation layer. The top of the saltation layer is situated at the interface between the water and sediment layers. Assuming that the top of the saltation layer has an elevation of z_{b} (i.e., bed elevation), the Exner-Polya equation governs the temporal variations of the bed elevation, as follows [68]:

$$(1-\gamma)\frac{\partial z_{\mathrm{b}}}{\partial t} + \nabla \cdot \boldsymbol{q}_{\mathrm{BL}} = \Phi \tag{8}$$

where γ represents the sediment porosity (=0.4), ∇ is the divergence operator, and $\boldsymbol{q}_{\mathrm{BL}}$ is the bedload flux vector. Φ is the net volume flux of vertical sediment transport across the water-sediment interface. Assuming that the sediment transport is confined to the saltation layer and there is no vertical sediment transport, the right-hand side of Eq.(8) reduces to zero. At the interface of the sediment and water, the bedload flux vector is obtained by the following equation [10]:

$$\boldsymbol{q}_{\mathrm{BL}} = \psi \, \|d_{\mathrm{s}}\| \, \|\delta_{\mathrm{BL}}\| \, \boldsymbol{u}_{\mathrm{BL}} \tag{9}$$

where $\boldsymbol{u}_{\mathrm{BL}}$ represents flow velocity parallel to the bed surface, d_{s} is the edge length of each of the bed's unstructured triangular grids, and ψ is the sediment concentration in the bedload layer. The sediment concentration over the water-sediment interface and at each cell center is calculated deterministically, as follows [69] :

$$\psi = 0.015 \frac{d_{50}}{\delta_{\mathrm{b}}} \frac{T^{3/2}}{D_*^{3/10}} \tag{10}$$

$$D_* = d_{50} \left[\left(\frac{\rho_{\mathrm{s}} - \rho}{\rho \nu^2} \right)^{1/3} \right] \tag{11}$$

where ρ_{s} is the sediment density (=1920 kg/m^3), ν is the fluid's kinematic viscosity, and g is the gravitational acceleration. T denotes excess shear stress, which is calculated as

$$T = \frac{\tau_* - \tau_{*\mathrm{cr}}}{\tau_{*\mathrm{cr}}} \tag{12}$$

where $\tau_{*\mathrm{cr}}$ is the critical shear stress initially obtained for a flatbed [69], which receives appropriate corrections for longitudinal and transverse bed slopes [9]. τ_* represents the bed shear stress obtained through the wall model [9]. To determine the velocity and shear stress at the nearest grid nodes adjacent to the wall nodes, also known as immersed boundary (IB) nodes, situated at the sediment-water interface, we adopt the wall model approach [9, 10]:

$$\frac{u}{u_*} = \begin{cases} y^+ & y^+ \leq 11.53 \\ \frac{1}{\kappa} \ln\left(E y^+\right) & y^+ > 11.53 \end{cases} \tag{13}$$

where u is the local velocity magnitude at the distance y from the wall, u_* represents the shear velocity, and y^+ $(= y u_*/\nu)$ is the dimensionless distance from the wall. Additionally, κ is the von Kármán constant (=0.41 in this work), and E is the roughness parameter which is defined by the subsequent equation:

$$E = \exp(\kappa(B - \Delta B)) \tag{14}$$

where $B = 5.2$ is the additive constant, and ΔB defined as follows:

$$\Delta B = \begin{cases} 0 & \text{if } k_{\mathrm{s}}^+ < 2.25 \\ \left[B - 8.5 + (1/\kappa)\ln(k_{\mathrm{s}}^+)\right] \sin\left[0.4258\left(\ln(k_{\mathrm{s}}^+) - 0.811\right)\right] & \text{if } 2.25 < k_{\mathrm{s}}^+ < 90 \\ B - 8.5 + (1/\kappa)\ln(k_{\mathrm{s}}^+) & \text{if } k_{\mathbf{s}}^+ \geq 90 \end{cases} \tag{15}$$

where $k_{\mathrm{s}}^+ = k_{\mathrm{s}} u_*/\nu$ and k_{s} is the effective roughness height of the boundary; that is, of the water-sediment interface. For mobile beds, k_{s} is commonly assumed to be greater than d_{50} [10]. In this work, we consider $k_{\mathrm{s}} = 3d_{50}$.

Upon obtaining all parameters at the cell centers, the GAMMA scheme transfers them to the cell faces [9]. A physical constraint in the numerical model is the need to correct each unstructured grid's slope if it exceeds the sediment material's angle of repose. In this case, the sand's angle of repose is 40°. The sand-slide model utilized by [8, 10, 12] addresses this constraint. At each simulation iteration, the sand-slide model identifies the unstructured cells with slopes exceeding the angle of repose. When the model detects such a slope, it balances the mass distribution between the identified and neighboring cells. Then, the algorithm redistributes the mass between these cells to prevent the cells' slope from exceeding the angle of repose by sliding down the excess slope equal to the angle of repose and by satisfying mass conservation [8]. The sand-slide algorithm iterates until the maximum slope of the bed reaches 99% of the angle of repose of the sediment material [8].

For the sediment transport computations around bluff bodies such as MHK turbine towers, a correction factor is generally used in the RANS model to increase the accuracy of the scour prediction [11]. Hence, we attempt to improve the sediment transport prediction of the RANS model by incorporating an effective bed shear stress ($\tau_{\text{effective}}$), which is a corrected form of the shear stress obtained from the wall model (τ_0). The effective bed shear stress is given by [70]:

$$\tau_{\text{effective}} = \tau_0 + \tau_{\text{extra}} \tag{16}$$

where τ_{extra} accounts for the additional shear stress resulting from the interaction between the flow and the upstream edge of the MHK turbine structure. This term can be found by the following equation [70, 71]:

$$\tau_{\text{extra}} = \frac{5}{24} C_{\text{e}} \rho ||\hat{w}|| \hat{k} \tag{17}$$

where C_{e} is a constant equal to 1.5. The value of $\hat{k}$ is computed from depth-averaging the turbulence kinetic energy, k (obtained from $k-\omega$ model), over the lower half of the flow depth above individual bed elements, while $\hat{w}$ is determined as follows [11]:

$$\hat{w} = \frac{\widetilde{w}}{\sqrt{u^2 + v^2 + \widetilde{w}^2}} \tag{18}$$

where u and v denote the flow velocity components at the edge of the bed load layer, which are parallel to the bed. The wall-model approach calculates these velocity components. Additionally, $\widetilde{w}$ denotes the bed-perpendicular velocity component, which is as follows [11]:

$$\widetilde{w} = \frac{\left(w - u\frac{\partial z}{\partial x} - v\frac{\partial z}{\partial y}\right)}{\sqrt{\left(\frac{\partial z}{\partial x}\right)^2 + \left(\frac{\partial z}{\partial y}\right)^2 + 1}} \tag{19}$$

where $x,\ y,\ z$ respectively signify the streamwise, spanwise, and vertical directions, while w denotes the depth-averaged velocity component of the flow over the lower half of the flow depth.

2.3. The hydro- and morpho-dynamics coupling

Coupling of morphodynamics with hydrodynamics involves separate solutions in their respective domains. However, to account for their interaction, a new boundary condition is applied at the interface of sediment-water [12]. To achieve this, we employ the partitioned loose-coupling fluid-structure interaction (FSI) approach [8, 10, 12]. The FSI for arbitrarily complex moving and stationary geometries is handled using the curvilinear immersed boundary method (CURVIB). The CURVIB method discretizes solid surfaces into unstructured triangular grid systems immersed within structured background grid systems (see, for more details, [50, 63]). When solving the hydrodynamic equations, we consider the mobile bed's geometry and the bed surface's vertical velocity as the boundary conditions. On the other hand, we use the shear stress and velocity field at the sediment-water interface to solve the governing equations of bedload layer [12].

An important consideration in the hydro- and morpho-dynamic coupling is the disparity in convergence timescales between flow dynamics and morphodynamic processes. While the flow convergence may occur within seconds or minutes, achieving bed equilibrium could take days or weeks. This discrepancy is addressed using different time steps for the flow solver and the morphodynamic solver. Namely, herein, the time step used for the morphodynamic solver is two orders of magnitude greater than that of the flow solver [7].

Overall, the hydro- and morpho-dynamics coupling procedure can be summarized as follows: First, the flow governing equations (Eq.(1) and Eq.(2)) is solved for time step $n+1$, with the known information about mobile bed geometry and bed surface vertical velocity at time step n. Then, the morphodynamic equations (Eq.(8) to Eq.(12)) are solved to calculate the new bed geometry at time step $n + 1$. Third, the sand-slide model is applied for those cells with a slope higher than the angle of repose. Finally, the modified bed geometry, as well as the bed surface vertical velocity, are used as boundary conditions for solving the governing equations of the flow for time step $n + 2$. More details are available in Refs. [7, 12].

2.4. The ALN model

The actuator line works by parameterizing each of the MHK turbine's blades as straight, rotating lines, thereby yielding forces as source terms to the RHS of the momentum equations (Eq.(2)). First, each blade is divided into radial segments. Next, drag and lift forces are respectively obtained as follows:

$$F_{\mathrm{D}} = \frac{1}{2} c \rho C_{\mathrm{D}} V_{\mathrm{rel}}^2 \tag{20}$$

$$F_{\mathrm{L}} = \frac{1}{2} c \rho C_{\mathrm{L}} V_{\mathrm{rel}}^2 \tag{21}$$

where C_{D} and C_{L} are the drag and lift coefficients, respectively. These coefficients are functions of Reynolds number and the angle of attack [55]. c represents the chord length. Before introducing relative incoming velocity (V_{rel}), we define the flow velocities averaged over the actuator line in the axial (u_x) and azimuthal directions (u_θ), as follows [72]:

$$u_x = \boldsymbol{u}(X) \cdot \boldsymbol{e}_x \tag{22}$$

$$u_\theta = \boldsymbol{u}(X) \cdot \boldsymbol{e}_\theta \tag{23}$$

Here and in the following equations, x_i and X_i ($i = 1, 2, 3$, in compact tensor notation) correspond to the Cartesian coordinate system for fluid grid nodes and the Lagrangian coordinate system for actuator lines, respectively. $\boldsymbol{e}_x$ and $\boldsymbol{e}_\theta$ are unit vectors in the axial and azimuthal directions, respectively. The velocity on the actuator lines comes from interpolating the background velocity at the grid notes. The interpolation involves the discrete delta function (δ_h) in the following manner [72]:

$$\boldsymbol{u}(X) = \sum_{N_f} \boldsymbol{u}(\boldsymbol{x})\delta_h(x - X)V(x) \tag{24}$$

where $V(x)$ represents each fluid cell's volume, and N_{f} denotes the total number of fluid cells [72]. Delta function is defined as [73]:

$$\delta_h(x - X) = \frac{1}{V}\phi\left(\frac{x - X}{h_x}\right)\phi\left(\frac{y - Y}{h_y}\right)\phi\left(\frac{z - Z}{h_z}\right) \tag{25}$$

where ϕ is the smoothed four-point cosine function [55].

It is also necessary to consider the effects of the tip loss and the corrected drag and lift coefficients [55]. Once u_x and u_θ are obtained, incoming velocity (V_{rel}) is determined as follows [72]:

$$V_{\mathrm{rel}} = (u_x, u_\theta - \Omega r) \tag{26}$$

where r is the distance from the blades to the rotor center and Ω is the rotor rotational speed. After computing the incoming velocity and the drag and lift forces (Eq.(20) and Eq.(21)), the distributed body force acting on the fluid nodes, which is related to the source term on the RHS of Eq.(2), is obtained by the following equation [72]:

$$f_{\mathrm{AL}}(x) = \sum_{N_{\mathrm{f}}} f(X)\delta_h(x - X)A(X) \tag{27}$$

where $A(X)$ represents the divided actuator line's segmented length. The current study assumes the force to be uniformly distributed over the chord length. Hence, the force per unit area ($f(X)$)

can be obtained from the given equation [72]:

$$f(X) = \frac{(F_{\mathrm{L}} + F_{\mathrm{D}})}{c} \tag{28}$$

Additionally, the actuator line model for rotating blades integrates with the representation of the nacelle. Parameterization of the nacelle element of the turbine entails accounting for distributed friction forces across its surface. Such forces are computed as tangential and normal force components over the nacelle surface with the respective equations [50].

$$f_{\mathrm{n}} = \frac{h\widetilde{u_{\mathrm{n}}}}{\Delta t} \tag{29}$$

$$f_{\tau} = \frac{1}{2}\rho C_{\mathrm{f}} U_{\infty}^{2} \tag{30}$$

where $h = (\Delta x \Delta y \Delta z)^{\frac{1}{3}}$ is the length scale of the Eulerian grid, and $\widetilde{u_{\mathrm{n}}}$ denotes the velocity normal to the actuator surface of the nacelle. C_{f} represents the friction coefficient, which is determined through the following empirical relation [50]:

$$C_{\mathrm{f}} = 0.37\,(logRe_{x}) - 2.584 \tag{31}$$

where computed Reynolds number, Re_x, is determined based on the incoming velocity and the distance from the leading edge of the nacelle. After obtaining the individual forces, they are projected onto the Eulerian grid through a smoothed cosine discrete delta function, Finally, they are integrated into Eq.(2) as an external force.

We should note that the flow solver and sediment transport model have been extensively validated through many studies (see, e.g., [7–12, 32, 35, 67, 74]). In Section Appendix A, we also present a recent validation study in which the flow solver is further validated against experimental data reported in Kang et al. [75].

3. Test case description and computational details

In this section, we present details of the test case and numerical experiments involving a virtual utility-scale MHK turbine with various configurations of woody debris accumulations under rigid and live bed conditions. The turbine is installed in 25 m wide, 87.5 m long, and 7.8 m deep flume (Fig. 1). The approaching flow velocity (U_∞) is 1.56 m/s and the turbine rotor's diameter is 5 m, resulting in a Reynolds number of 7.8×10^6 (Table 1).

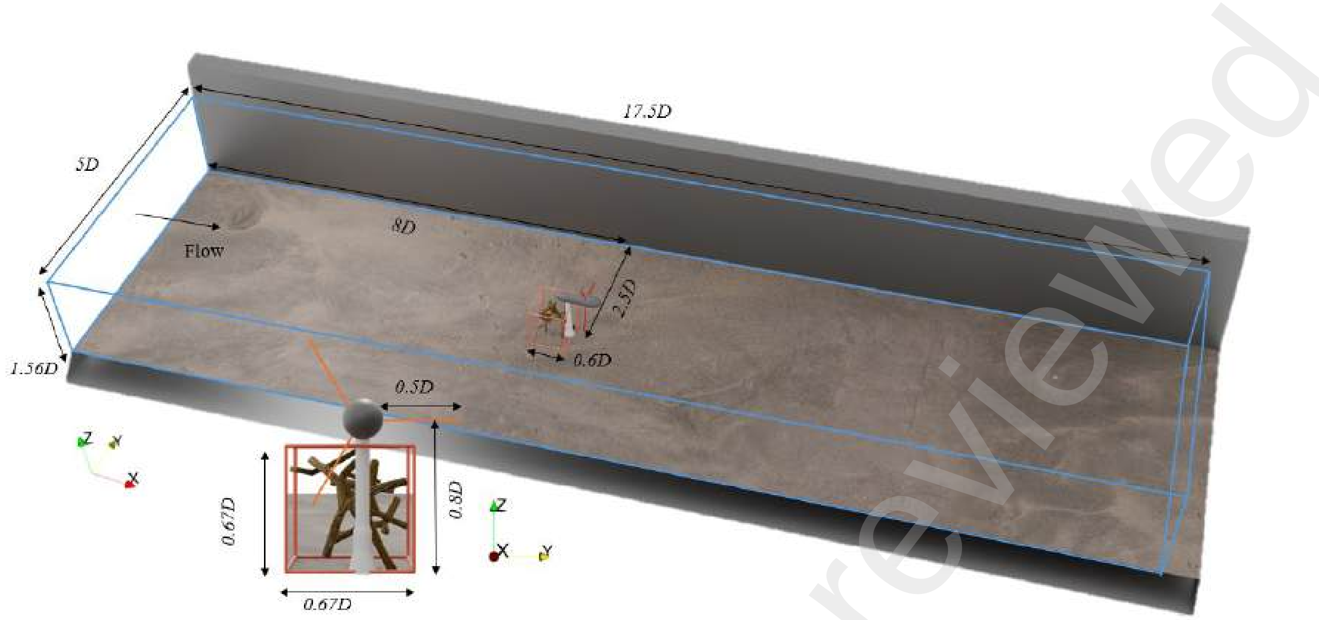

Fig. 1. The layout of the channel, MHK turbine, and impermeable box. The dimensions are normalized with the rotor diameter (D = 5 m). The MHK turbine has a hub height of 0.8D and is located 8D downstream from the channel inlet. The flow direction is represented as positive along the x-axis, and the z-axis denotes the vertical direction. The impermeable box dimensions are 0.6D in length and 0.67D in width and height. The channel spans a length of 17.5D, with a width of 5D, and the flow depth is noted as 1.56D.

The modeled MHK turbine is constructed using the Gen4 Kinetic Hydropower System (KHPS) design, which was developed by Verdant Power Inc. The turbine, modeled using the ALN method at a constant tip-speed ratio (TSR) of $\lambda = 2.5$, was stationed at 8D downstream from the channel inlet and has a hub height of 0.8D.

Furthermore, the woody logs for debris accumulation cases were selected based on different shapes and sizes of the same model of truncated willow trees containing the trunk and major limbs. The diameter and length of the selected woody logs range from 2 cm to 10 cm and 0.2 m to 3.6 m, respectively. The digital map of the woody logs and their random accumulations was created using the Blender open-source software. To replicate natural conditions, we established six virtual debris configurations randomly piled against the turbine's upstream side (Fig. 2). A configuration without a debris pile is the baseline case, also known as case 0.

Table 1: Details of the flow, turbine, and the mobile bed. H, U_∞, and D represent the water depth, the incoming velocity, and the diameter of the utility-scale MHK turbine, respectively. Re_{D} is the Reynolds number based on the diameter of the turbine. λ denotes the tip-speed ratio of the blade. The mobile bed characteristics include d_{50}, ρ_s, and γ, representing the sediment material's median grain size, grain density, and porosity, respectively.

H (m)	U_∞ (m/s)	D (m)	Re_{D}	λ	d_{50} (mm)	ρ_s (kg/m^3)	γ
7.8	1.56	5	7.8×10^6	2.5	1	1920	0.4

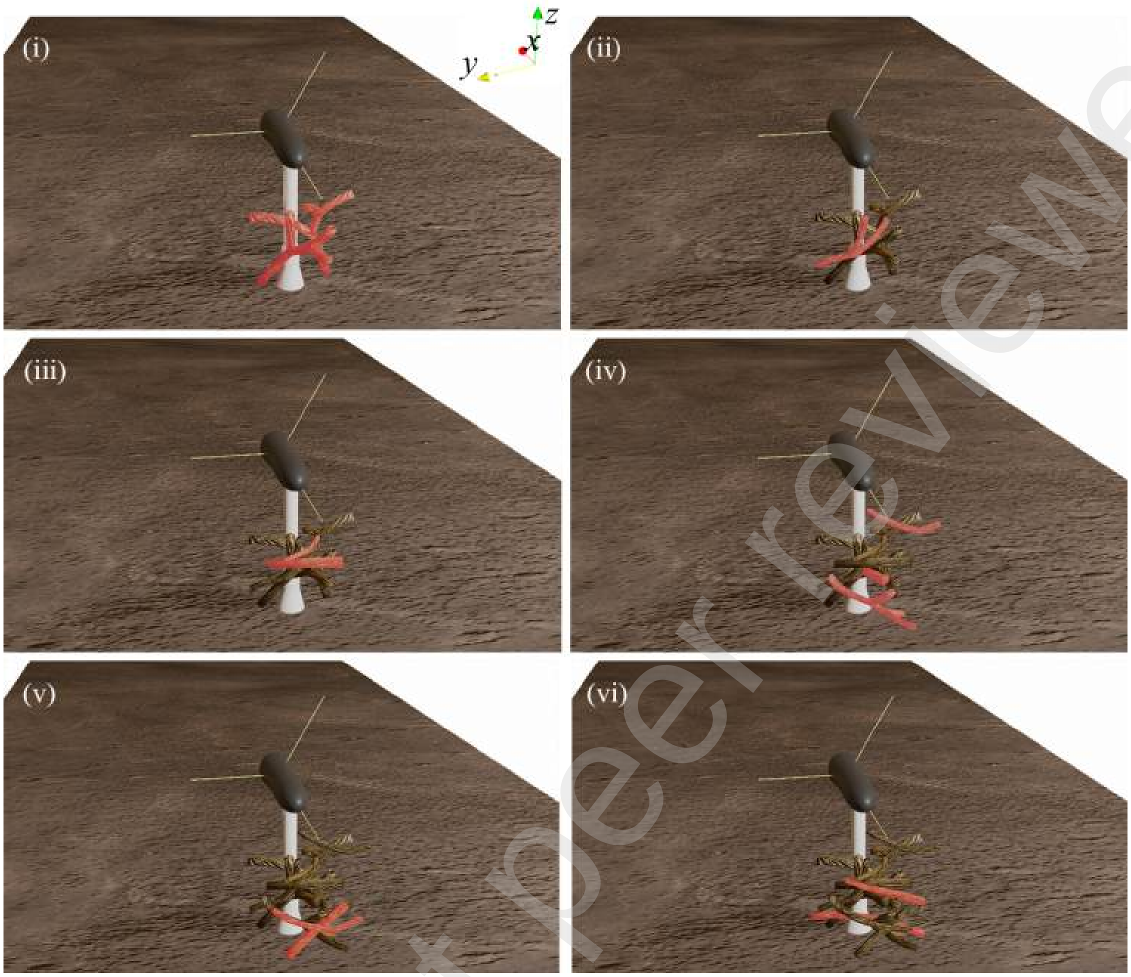

Fig. 2. Digital map of the debris accumulations used in the simulations. The degree of debris cluster increases from cases 1 to 6, while case 0 refers to the benchmark test bed with no debris accumulation. Yellow lines represent the blades, and the surface representation of the nacelle is dark metallic gray. The successively added woody logs from case 1 (i) to case 6 (vi) are marked in red.

As seen in Fig. 2, we systematically and gradually added woody branches to the upstream face of the turbine tower, creating debris accumulation cases numbered 1 to 6. The number of woody logs in the debris piles, the relative porosity, and the blockage ratio (i.e., percentage of the surface area perpendicular to the streamwise flow to the cross-section of the flume) of each case are outlined in Table 2. The relative porosity ($\%100 \times (1 - V_{\mathrm{dr}}/V_{\mathrm{ref}})$) describes the percentage of volume of the cluster (V_{dr}) occupied in assumed impermeable box volume (V_{ref}), as shown in Fig. 1.

Furthermore, the sediment material considered in the mobile bed simulations was composed of uniformly graded non-cohesive sand (see Table 1). In the simulations under live bed conditions, we first ran the turbulent flow in the flume with frozen flat beds. Once the instantaneous flows were statistically converged, we activated the bed morphodynamics module of the code, allowing for bed deformations. The convergence of the instantaneous flow field was examined by monitoring the time history of the total kinetic energy within the flow domain.

Table 2: Parameters of debris accumulation cases 1 to 6. The blockage ratio denotes the ratio between the blocked area and the channel's cross-sectional area. Porosity is defined as the ratio of the debris accumulation volume to the box volume, as demonstrated in Fig. 1.

Case	0	1	2	3	4	5	6
Number of logs in pile	0	2	3	5	8	10	12
Porosity (%)	100	98.63	98.40	98.14	97.48	97.14	96.70
Blockage ratio (%)	0	0.24	0.29	0.34	0.45	0.53	0.59

Based on a grid sensitivity analysis, reported in Section Appendix B, the flume's computational domain was discretized by approximately 19 million computational grid nodes, with a non-dimensional uniform resolution ($\Delta x_i/D$) of 0.02 in all directions (Table 3). The non-dimensional time step was selected to ensure that the maximum Courant Friedrichs Lewy number remained below 1.0.

A wall model approach was employed to incorporate the hydrodynamic effects of solid surfaces (e.g., the sidewalls, channel bed, woody debris, and turbine components) on the flow. The solid surfaces were modeled as hydraulically smooth wall boundaries. The water surface was modeled with a rigid-lid assumption, while Neumann boundary conditions were applied at the outlet cross-section. A precursor simulation with periodic boundary conditions – in the streamwise direction – was performed to obtain a fully developed turbulent open-channel flow to be imposed at the flume's inlet. The transient developing boundary layer of the precursor simulation was discarded until the total kinetic energy reached a quasi-steady state. Subsequently, the instantaneous velocity fields of the precursor simulation were recorded on a cross-sectional plane. The obtained flow field was imposed at the inlet of the flume as the inlet boundary condition. Further, the outflux of the sediment within the bedload layer and at the flume's outlet was numerically collected and fed into the flume at the inlet.

Table 3: Details of the computational grid systems and time steps for the flow and morphodynamics solvers. N_x, N_y, and N_z are the number of computational grid nodes in the streamwise, spanwise, and vertical directions, respectively. Δx, Δy, and Δz are spatial steps of the flow solver normalized with the rotor diameter, D. Δs is the spatial step of the morphodynamics solver normalized with D. Δz^+ is the minimum grid spacing in the vertical direction scaled by inner wall units. $\Delta t = t(U_\infty/D)$ is the flow solver's non-dimensional time step, where t is the dimensional time step. $\Delta t_s = t_s(U_\infty/D)$ is the non-dimensional time step of the sediment transport computations, where t_s is the dimensional time step.

Variable	Grid
N_x, N_y, N_z	$881 \times 253 \times 81$
$\Delta x, \Delta y, \Delta z$	0.02
Δz^+	1000
Δs	0.03
Δt	0.001
Δt_s	0.1

Finally, the numerical simulation for each case was carried out with 96 processors on a Linux cluster (AMD Epyc). On average, 12,000 CPU hours were required for the cases with the rigid bed to reach statistically converged flow fields. Meanwhile, the mobile bed simulations using the coupled flow and morphodynamics model required an average of 47,000 CPU hours to reach equilibrium bed topology, nearly quadrupling the time needed for the rigid bed simulations.

4. Result and discussions

We first discuss the turbine's wake flow field results under rigid bed conditions, followed by the mobile bed simulation results with various degrees of debris accumulation. Next, we analyze the wake recovery of the rigid and mobile bed simulations. Finally, we present the power production results and assess the impact of sediment transport and debris accumulation on the MHK turbine's power production and efficiency.

4.1. Wake flow under rigid bed conditions

In Fig. 3, we plot the instantaneous iso-surfaces (= 18) of the Q-criterion from a side view and in 3D for various degrees of woody debris accumulations. The iso-surfaces are colored with their elevation from the rigid bed ($z/H = 0$, where H is the flow depth) to the water surface at $z/H = 1$. Most visualized vortical coherent structures are located in the turbine's wake. The tip vortices can be observed extending from shallow to deeper regions of the flow depth, while most coherent flow structures are shed from the logs. More specifically, the tip vortices are observed to reach as high as $0.85H$. On the other hand, in the near bed regions, the tip vortices are distorted due to interference with debris buildup and the tower. As the density of the logs increases, from case 1 to case 6, the vertical flow structures become more pronounced. Apart from this general trend of coherency, Figure 3 reveals that the shear layers traveled farther downstream as debris cluster density increases, elongating the wake region. This can be clearly seen by comparing the side views of case 3 (Fig. 3(iii)) and case 6 (Fig. 3(vi)) where a denser debris accumulation induces intricate vertical flow structures under the cluster and in the mid-region of the turbine wake. Furthermore, a series of less pronounced near-bed vertical structures can be observed over the entire rigid bed of the flume. These flow structures and the corresponding sweep and ejection events they induce are expected to lead to heterogeneous bed deformations on the mobile bed [48].

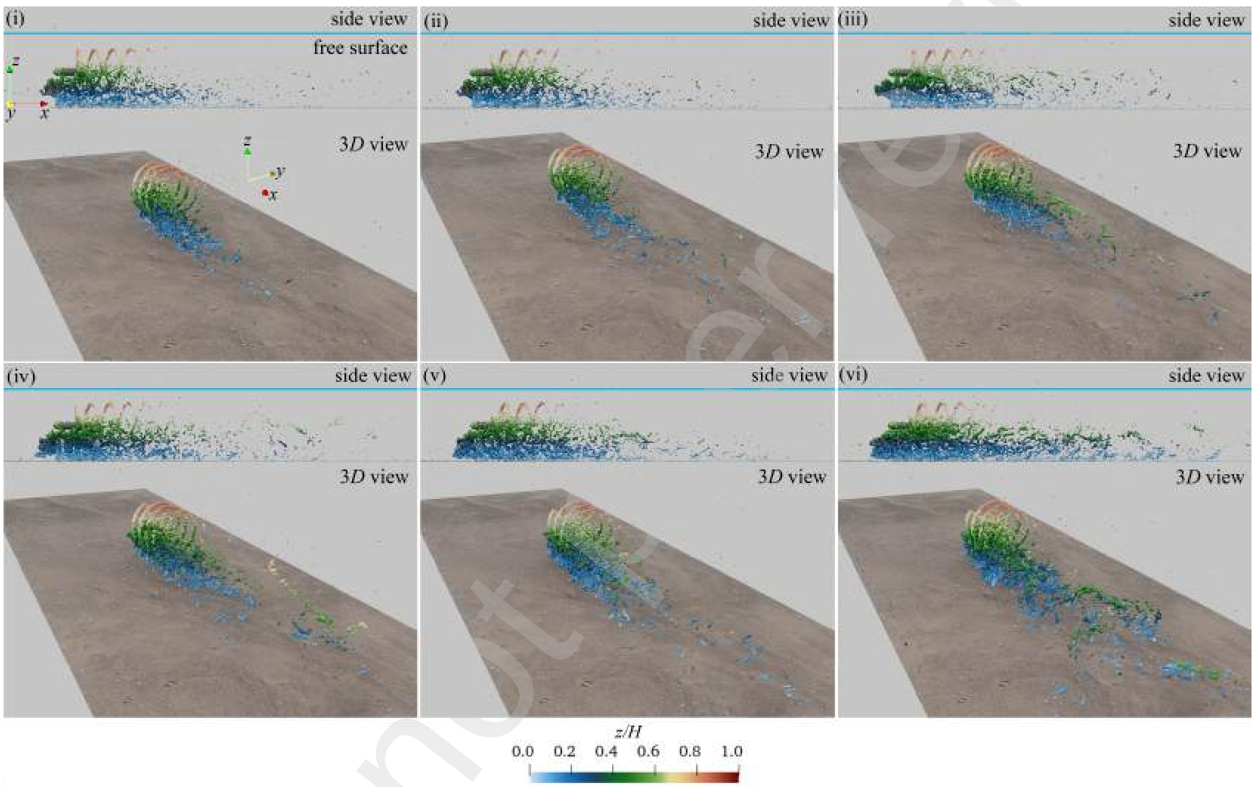

Fig. 3. LES-computed instantaneous vertical flow structures visualized with the iso-surfaces of the Q-criterion (=18) for cases 1 (i), 2 (ii), 3 (iii), 4 (iv), 5 (v), and 6 (vi) of debris cluster under rigid bed conditions from the side and 3D views. The iso-surfaces are colored with elevation from the bed at $z/H = 0$ to the water surface $z/H = 1$. In the side views, the light blue line refers to the free surface.

We continued the LES to obtain statistically converged turbulence statistics of the wake flow for all test cases. In Fig. 4, we plot the contours of mean streamwise velocity and turbulence kinetic energy from different points of view. In this figure, the color map of the mean streamwise velocity is plotted on a vertical plane at the channel's centerline while the color maps of the turbulence kinetic energy are depicted on the vertical and horizontal planes. It should be noted that the top row of pictures in this figure, i.e., Fig. 4(i) to (iii), corresponds to case 0, which includes no debris cluster, and thus provides a benchmark case. As seen, the results of case 0 mark a typical momentum deficit map in the wake of the turbine components. However, the gradual addition of logs onto the upstream face of the tower modulates the panorama of the mean flow statistics and momentum deficit. Once again, we note that the addition of woody logs in cases 1 to 6 was done haphazardly to mimic the natural positioning of the debris logs over the face of the tower. As a result, from cases 1 to 6, the blockage area and density of the woody cluster successively increase while the porosity and the opening between individual logs decrease.

As seen in Fig. 4(iv) to (xxi), the gradual increase of debris accumulation leads to a constant rise in the size and intensity of the momentum deficit in the wake of the turbine. However, a careful examination of mean streamwise flow in Fig. 4(x) and (xiii) indicates the existence of some form of through-canopy jet flow, owing to the openings between the logs, which contributes to the wake recovery. As the density of the woody debris increases, these random openings between individual logs disappear. As a result, such through-canopy jet flows no longer exist (or are markedly diminished) in cases 5 and 6 with dense debris accumulation. However, as seen in Fig. 4(xvi) and (xxi), the greater blockage effect of the debris in cases 5 and 6 gives rise to the formation of some sort of sub-canopy jet flows which form beneath the debris cluster. Notwithstanding the presence of various random jet flows within and around the debris cluster induced by various degrees of log density, the accumulation of woody branches seems to modulate the wake deficit of the turbine significantly. This modulation could have important implications for the power production of the turbine and the sediment dynamics around it.

Moreover, the contour plots of the turbulence kinetic energy over the vertical plane at the channel's centerline (shown in the second column of Fig. 4) mark the increase of turbulence kinetic energy with the successive growth of the woody debris density. As the blockage effect of the debris augments, the high turbulence kinetic energy region extends downward, peaking near the bed. This increasing trend is specifically visible as we go from case 4 to case 6, as seen in Fig. 4(xiv) to (xvii) and down to (xx). The elevated turbulence kinetic energy extends to $2D$ downstream of the turbine tower. The near bed's peaking of turbulence fluctuations at high debris density and its footprint over the bed seems to be induced by the sub-canopy jet flow. According to Khosronejad et al. [11], the regions with elevated turbulence kinetic energy are strongly associated with the deep scour regions. Therefore, as discussed in the next section, such a marked increase of the turbulence kinetic energy in the near-bed region could lead to deep scour developments.

Further, the horizontal color maps of the turbulent kinetic energy, as seen in the third column of Fig. 4, show an asymmetrical distribution of the turbulence kinetic energy across the channel, as a result of the heterogeneous positioning and density of the woody debris cluster. We note that these horizontal planes are $0.2D$ above the rigid bed. As seen in case 6, with the greatest debris density, the elevated turbulence kinetic energy persists for nearly $6D$ downstream of the turbine. Overall, the successive augmentation of the wake flow's turbulence kinetic energy with woody debris density can be readily seen in the horizontal color maps of cases 0 to 6.

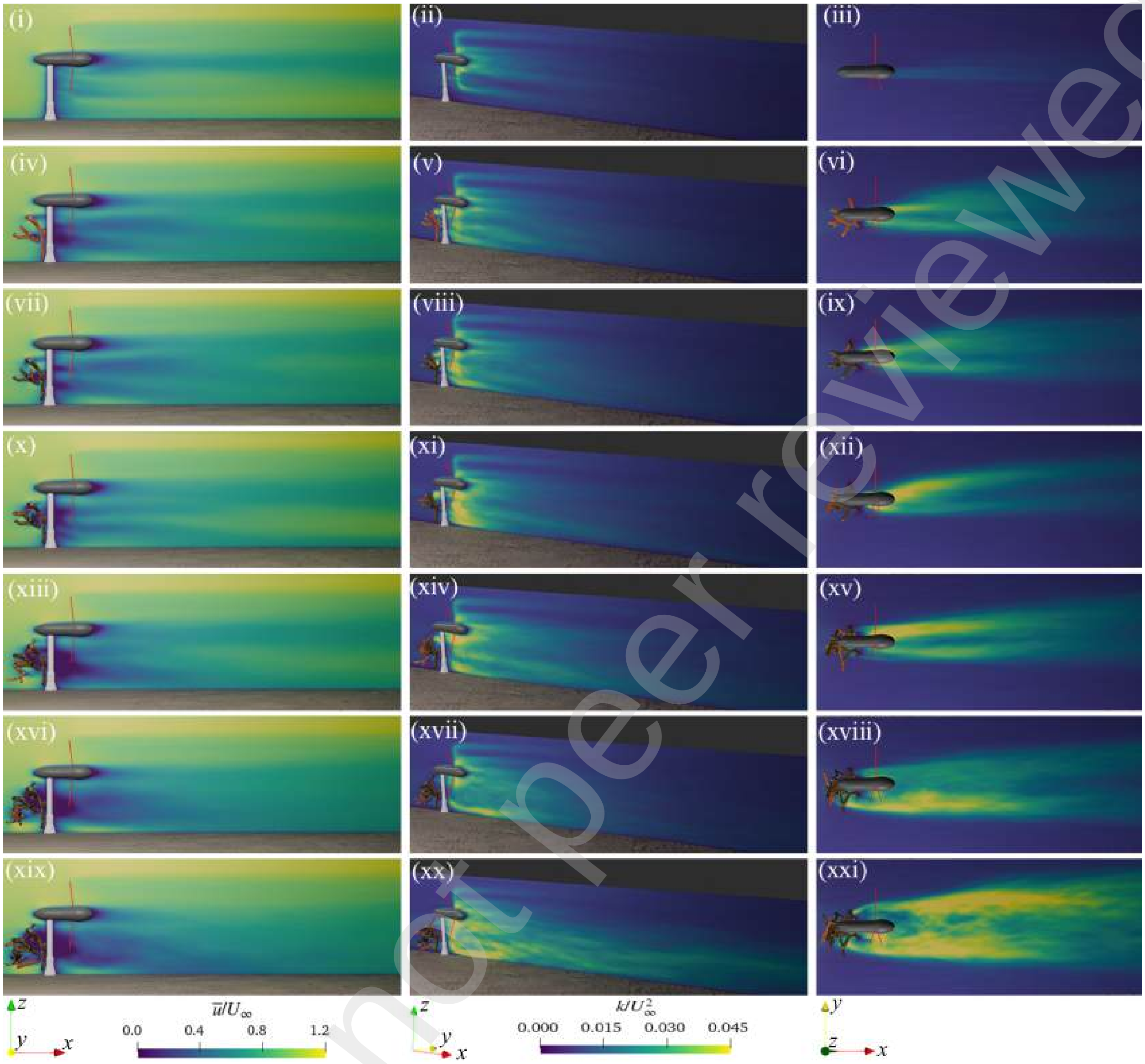

Fig. 4. LES-computed color maps of normalized mean streamwise velocity and turbulence kinetic energy under the rigid bed conditions. The pictures in the first to last row correspond to case 0 to case 6. Case 0 refers to the benchmark case with no debris, while case 6 corresponds to the maximum woody debris density test case. The first column depicts the contours of mean streamwise velocity on a vertical plane through the channel's centerline. The second and third columns show the contours of turbulent kinetic energy on a vertical plane through the channel's centerline and horizontal plane $0.2D$ above the bed, respectively.

4.2. Turbine wake flow and sediment dynamics under live bed conditions

In this section, we first present the hydrodynamics of the turbine with debris accumulation over the evolving bed topology of the channel and then discuss the morphodynamics of the mobile bed induced by the interaction of turbulent flow, rotating turbine blades, and debris accumulations. We note that the live bed condition is achieved by selecting appropriate hydraulic conditions and sediment properties, which leads to a flat-bed critical bed shear stress that is less than the bed shear

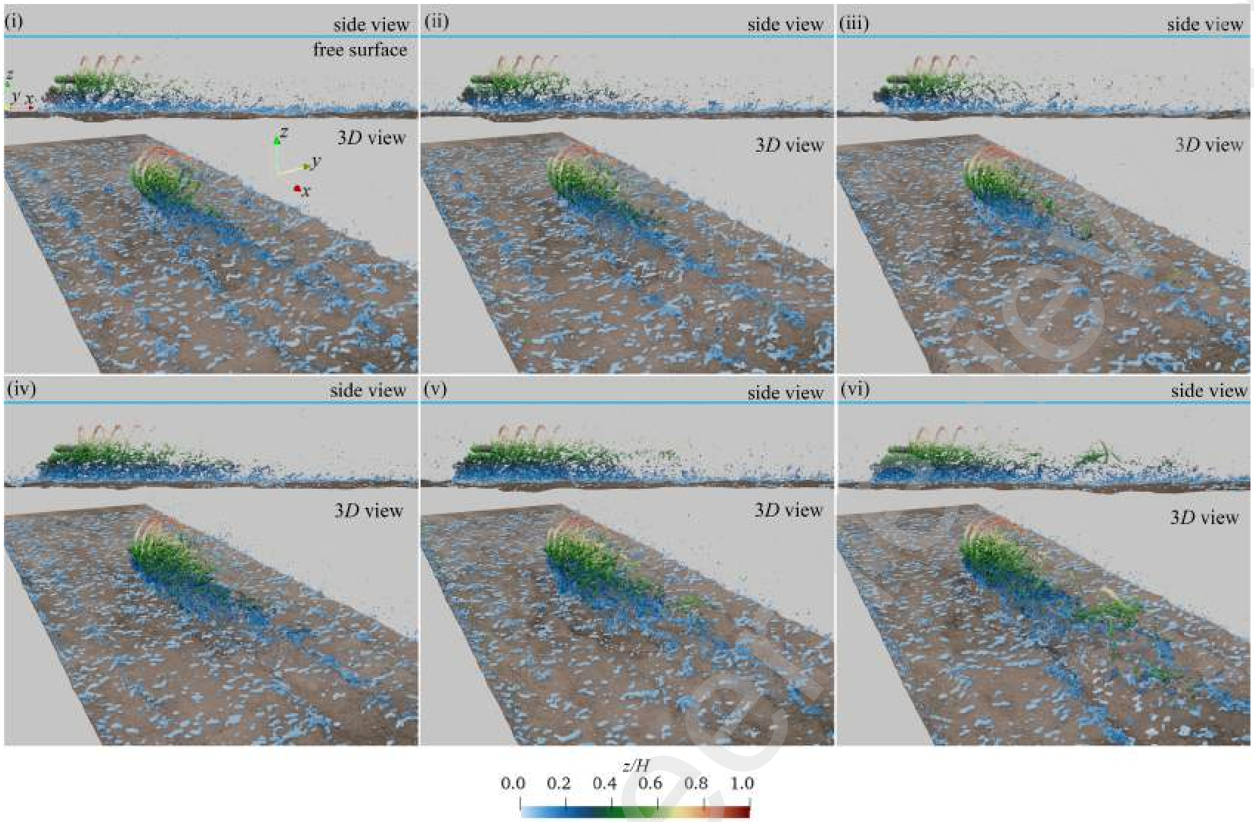

Fig. 5. LES-computed instantaneous vertical flow structures visualized with the iso-surfaces of the Q-criterion (= 18) for cases 1 (i), 2 (ii), 3 (iii), 4 (iv), 5 (v), and 6 (vi) of debris cluster under live bed conditions from the side and 3D views after the bed reached dynamics equilibrium. The iso-surfaces are colored with elevation from the bed at $z/H = 0$ to the water surface $z/H = 1$. In the side views, the light blue line refers to the free surface.

stress throughout the mobile bed of the flume. Under such conditions, as soon as the morphodynamics module of the code is activated, the existing bed shear stress induces initiation of motion, and the bed deformation commences throughout the channel.

4.2.1. Turbine wake flow under live bed conditions

Figure 5 plots the instantaneous the iso-surfaces of the Q-criterion (= 18) in cases 1 to 6. This figure illustrates the coherent flow structures and the bed morphology when the bed deformation throughout the channel for each case has reached its dynamic equilibrium state. Such an equilibrium state corresponds to a time when the maximum scour depth variation in the turbine's vicinity in two consecutive time steps is less than one percent. In other words, when at its dynamic equilibrium, the bed morphology still evolves, i.e., sand waves and other mobile bed features continue migrating and evolving, but the maximum scour depth stays relatively constant. The dynamic equilibrium time varies from case to case, but it was reached within an hour on average. The iso-surfaces are colored with their elevation above the initial flatbed ($z/H = 0$) to the water surface ($z/H = 1$). We note that at equilibrium, the bed deformation features - such as the sand waves and the deposition bar in the turbine's wake - are as high as 0.3 m to 0.5 m.

Compared to their counterpart under the rigid bed conditions in Fig. 3, the vertical flow structures seen in Fig. 5 near the bed surface throughout the channel are more energetic, as a consequence of the mobile bed's deformed geometry. We note that the near-bed coherent structures of the mobile bed at $t = 0$ closely resemble those present over the rigid bed (Fig. 3). However, the mobile bed's geometry begins to evolve soon after activating the code's bed morphodynamics module. The heterogeneous turbulence footprint over the bed surface causes the initial bed deformations. As the bed evolves, the sand waves, sand bars, and scour regions grow in size, forming greater and more energetic flow structures, like those seen in Fig. 5.

As discussed above, under the rigid bed conditions, the intensity and the extent of the turbulent flow structures became more pronounced with the density of the debris accumulation. Yet, such a trend is not as vividly observed under the live bed conditions (see Fig. 5 and Fig. 3). We argue that this is due to the role that the geometrical deformation of the bed plays in modulating flow instabilities and generating additional turbulence under the live bed condition. In other words, the constant deformation of the evolving bed surface induces instabilities that give rise to complex flow structures. As a result, over the mobile bed of the channel, the interaction among the turbine, woody debris, and the complex bed geometry is the determining factor to generate the vortical flow structures seen in Fig. 5.

We utilized the finite-time-averaged wake flow to elucidate the flow structures when the mobile bed is at a dynamic equilibrium state, i.e., the scour region fully develops in the turbine's wake. To that end, we plot in Fig. 6 the color maps of the finite-time-averaged mean streamwise velocity and turbulence kinetic energy over the bed when it reaches dynamics equilibrium. The finite-time-averaging results in this figure are obtained by freezing the deformed bed geometry at the equilibrium state, deactivating the morphodynamics module of the code, and averaging the instantaneous flow field over the frozen bed geometry. We note that the bed deformation features can be readily seen from the $3D$ views in the second column of this figure. The contribution of the bed deformation and relatively large bed features to the complex flow features becomes clearer in this figure. This figure shows that the migrating sand waves and the deposition bar in the wake region have grown large enough to modify the near-bed turbulence significantly.

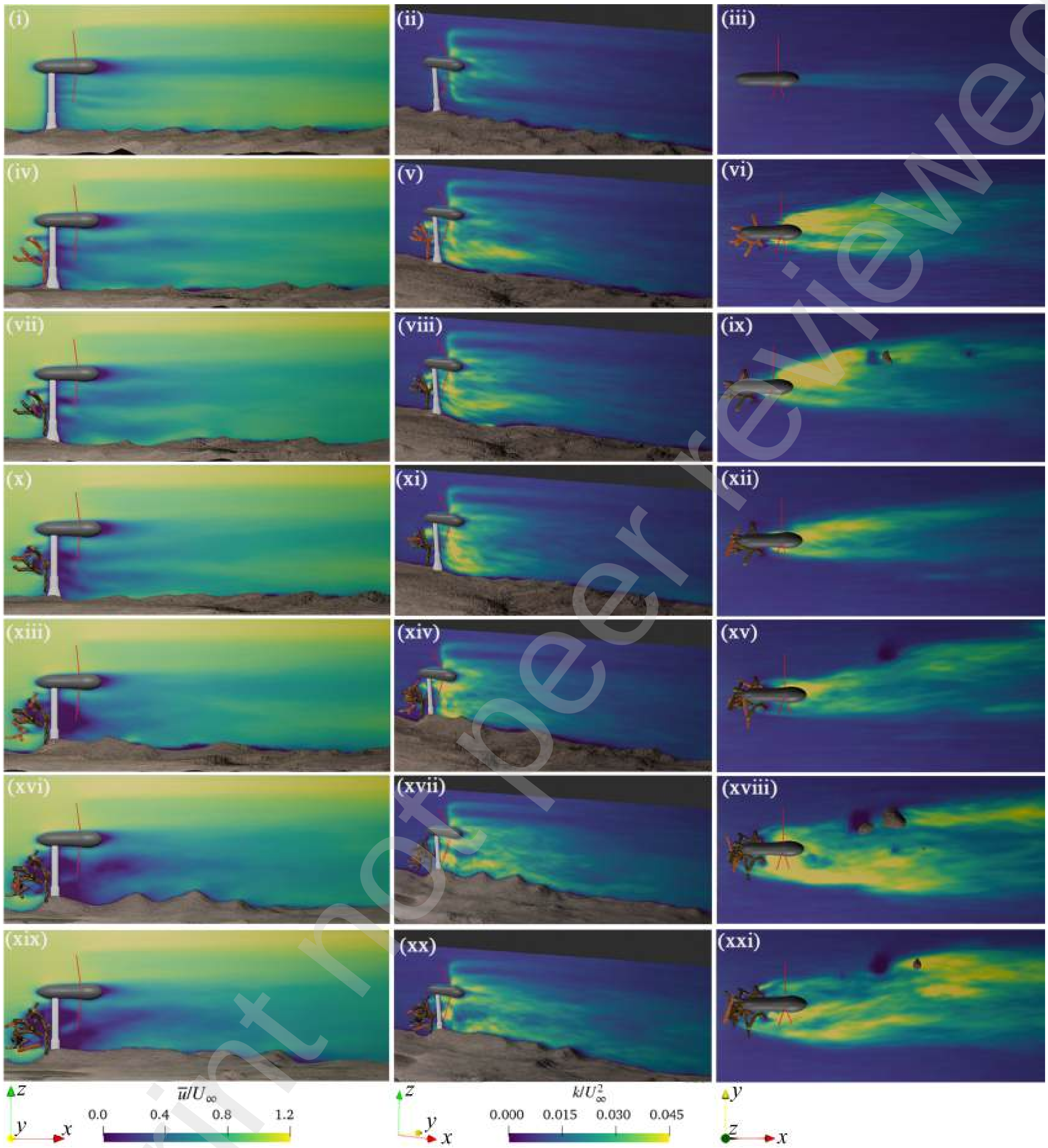

Fig. 6. LES-computed color maps of normalized mean streamwise velocity and turbulence kinetic energy under live bed conditions. The pictures in the first to last row correspond to case 0 to case 6. Case 0 refers to the benchmark case with no debris, while case 6 corresponds to the maximum woody debris density test case. The first column depicts the contours of mean streamwise velocity on a vertical plane through the channel's centerline. The second and third columns show the contours of turbulent kinetic energy on a vertical plane through the channel's centerline and horizontal plane $0.2D$ above the bed, respectively.

As seen in the contours of finite-time-averaged streamwise velocity (first column of Fig. 6), the wake momentum deficit of cases 4 to 6 is markedly increased as a consequence of the high density of the debris accumulation. Further, the wake flow is seemingly also impacted by the scour region and the sediment deposition bar in the wake region. More specifically, the sub-canopy jet flow, present in the rigid bed conditions, is less apparent in cases 4 to 6 of live bed conditions. The bed geometry in the turbine's wake is key in suppressing the sub-canopy jet flow. Thus, we argue that the bed geometry and the woody log density equally influence the momentum deficit. Needless to say, the bed geometry itself, at least in the near wake region, is impacted by the woody debris cluster as it modifies the turbulent flow. Then again, in cases with no or less density of the debris accumulation, e.g., cases 0 to 4, the momentum deficit is less impacted by the increase of the density of the debris clusters.In particular, from cases 1 to 3, the extent and intensity of the wake deficits seem to remain relatively unchanged. This is perhaps due to the interaction of the bed geometry and through-canopy jet flows within the debris clusters on the wake flow. As a result, we expect that the detrimental effect of the debris accumulation might less impact the power production and efficiency of the turbine under live bed conditions. In the next section, we will revisit this notion and investigate the impact of the live bed condition on the wake recovery and turbine efficiency.

Now, we focus on the finite-time-averaged results of the turbulence kinetic energy at the dynamic equilibrium state of cases with different debris cluster densities (the second and third columns of Fig. 6). Starting with case 0 in the first row of this figure, it is clear that in the absence of woody debris, the distribution of the turbulent kinetic energy resembles that of the rigid bed case except for the near-bed region where the effect of moving sand waves and the scour geometry under live bed conditions modifies the turbulence. For cases 1 to 6, the bed deformations, i.e., the sand waves and the scour/deposition regions, gradually grow in size, inducing stronger shear layers and bed shear stresses over the bed. The elevated shear stress and near-bed turbulence, in turn, exits the mobile bed even further. Overall, at their mature stage of development, the bed deformation drastically modulates the flow through this cycle, at least in the near-bed region. For instance, as seen in the third column of this figure, the size of the sediment deposition in the wake grows large enough to intrude into the horizontal planes at the elevation of $z/H = 0.2D$. As the shape of the mobile bed changes constantly, the topology and position of such intrusions, which are caused by sand deposition and sand waves, evolve in the wake region and throughout the channel.

Therefore, the complex interaction between the mobile bed and the turbulent flow gives rise to the asymmetrical turbulence kinetic energy distributions, as seen in this figure. Because of this intricate interaction, in the lower part of the flow depth, the turbulence kinetic energy distribution of cases 1 to 6 seems to be impacted by the variations of both the density of the debris cluster and bed deformation. For that, under live conditions, the wake region of the turbine for all cases is associated with almost equally high turbulence kinetic energy, and the variations in the debris density seem to be of less importance than the rigid bed conditions.

4.2.2. Turbine wake's sediment dynamics under live bed conditions

In Fig. 7, we plot the LES-computed instantaneous bed morphology of the channel for various debris accumulation densities. This figure's first row depicts the channel's RANS-computed temporal bed topography for case 0. This is the only coupled hydro-morphodynamics simulation we carried out using the RANS model to compare the two turbulence models using the same grid systems. As seen, the second row of this figure plots the LES results for case 0. Comparing the two rows, one can readily appreciate the differences in the bed morphodynamics computations of the two models. Namely, the LES has captured the scour and sediment deposition in the near wake region along with details of sand wave formation and migration throughout the channel. The RANS model has generated bed deformation near the turbine's wake, including in the scour and sediment deposition regions. Overall, although the predicted scour depths of the two models are nearly within the same range, the LES-predicted bed morphology seemingly contains many more geometrical details associated with various sand wave sizes sporadically scattered throughout the mobile bed of the flume.

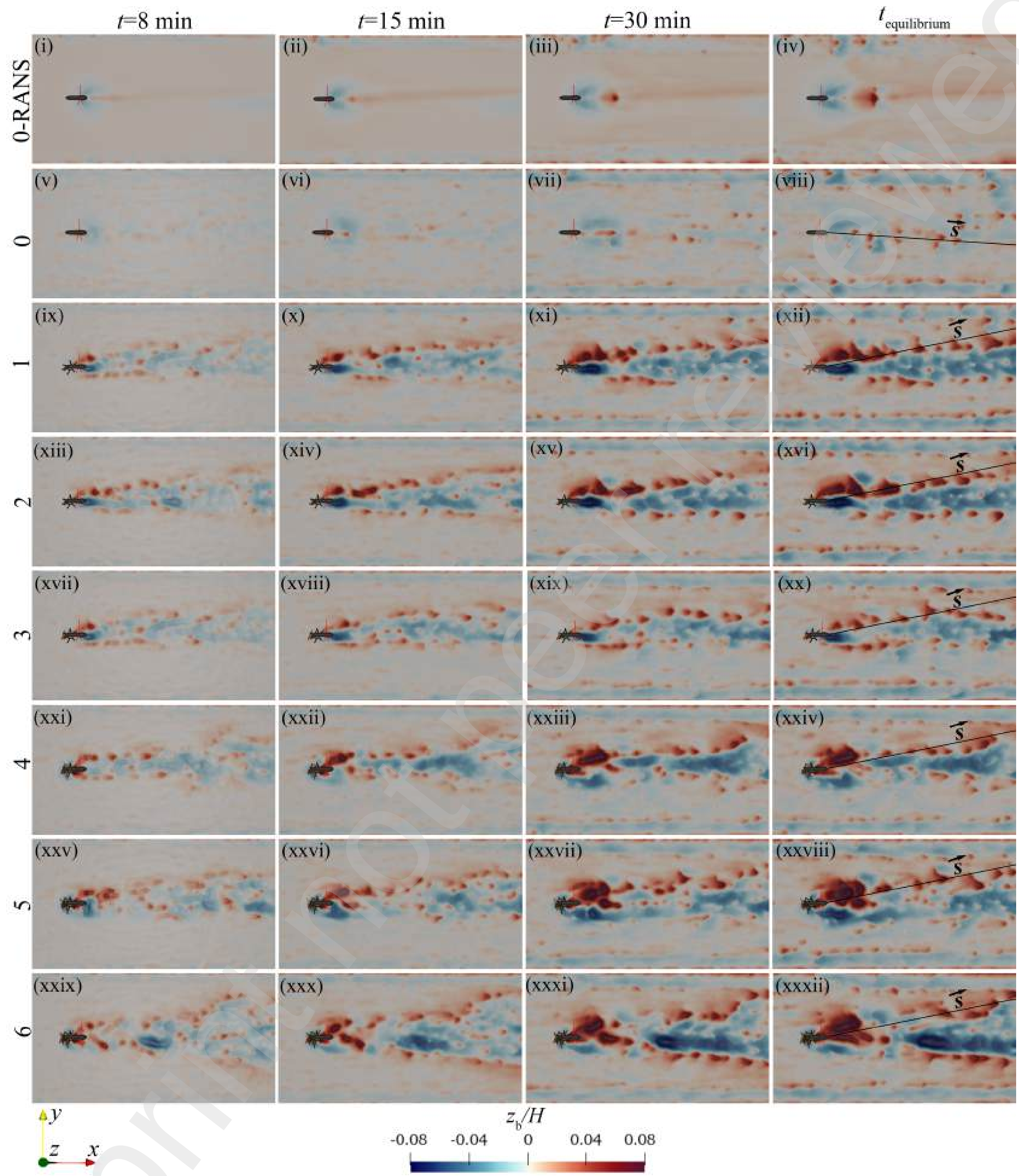

Fig. 7. Color maps of instantaneous bed elevation normalized with the water depth (=7.8 m) for cases 0 obtained using RANS model (first row) and cases 0 to 6 computed with LES model at instants t = 8 min (first column), 15 min (second column), 30 min (third column), and at equilibrium (last column). The bed geometries are shown from the top view. The case number of each row is shown on the left side of the figure. The time needed to reach the bed's equilibrium state is, on average, an hour.

Now, we focus on the LES-computed bed evolution of the channel for cases 1 to 6. Soon after the morphodynamics module is activated, the channel bed of cases 1 to 6 evolves, deviating from the initial flat bed. In all cases, the most dominant sand waves in amplitude and wavelength are generally initiated in the turbine's wake and propagate downstream. With time, these bedforms grow in size until they reach their equilibrium size. Further, they propagate downstream mainly along two lines that originate at the turbine wake toward downstream with an angle of roughly $\pm 11^0$ relative to the centerline, which conforms with the angle of the shear layer in the spanwise direction, as visualized by the contours of turbulence kinetic energy from top view (see third column of Fig. 6). The line along which the major sand waves form and migrate is denoted as vector '$\boldsymbol{s}$', which is marked with black lines over the equilibrium topography of Fig. 7 (third column). It is also observed that the topology of these sand waves is somewhat impacted by the random configurations/density of the debris clusters and the jet flow through the openings of the debris logs. For instance, the sand waves in case 3 have a smaller amplitude than those observed in cases 1 and 2, even though the density of the debris clusters in these cases is less than in case 3.

To further examine the LES captured bedforms, we plot in Fig. 8(i) the profiles of the bed elevation along the '$\boldsymbol{s}$' vector, as shown in Fig. 7. As seen, the initial portion, $s/D < 2$, of the bed profiles marks the scour hole developed in the near wake region of the turbines, where the turbine and debris clusters are located (the region between the two vertically drawn blue dotted lines in Fig. 8(i)). The deepest part of each profile in the near wake marks the effect of rotating blades. Apart from the initial portion of the profiles, the rest of the bed profiles demonstrate the formation of a series of mega ripples and dunes with a range of amplitudes and wavelengths. Given the range of the deformations' amplitude and wavelength (as discussed below and shown in Fig. 8(i)), the fluid, flow, and sediment material characteristics (as described in Section 3), these deforms range from mega ripples to dune [76]. As captured by the LES and shown in Fig. 8(i), such beforms types are categorized with smaller scale ripples superimposed over the larger scale dunes.

Additionally, Figure 8(ii) plots the mean normalized amplitude ($\overline{\Delta}_s/H$) and wavelength ($\overline{\lambda}_s/H$) of the LES-captured bedforms along '$\boldsymbol{s}$' vector. The mean amplitude and wavelength of the captured bedforms in different cases range from 0.18 m to 0.51 m and 3.6 m to 6.8 m, respectively. The amplitude of the bedforms has a general increasing trend from case 0 to case 6, which is consistent with the blockage ratio of the woody debris clusters. As the ratio of the blockage increases, the lateral shear layers caused by the debris accumulation increase, leading to the further acceleration of the flow and higher bed shear stress along the '$\boldsymbol{s}$' vectors, thus producing higher bedforms. However, as discussed above, the random logging of the individual logs and, therefore, their intricate openings/porosity induces strong jet flows through and beneath them. Such random arrangements, for example, in case 2, have led to bedforms with relatively higher amplitude than those in cases 3 and 4, even though the latter cases have higher blockage ratios than the former case 2.

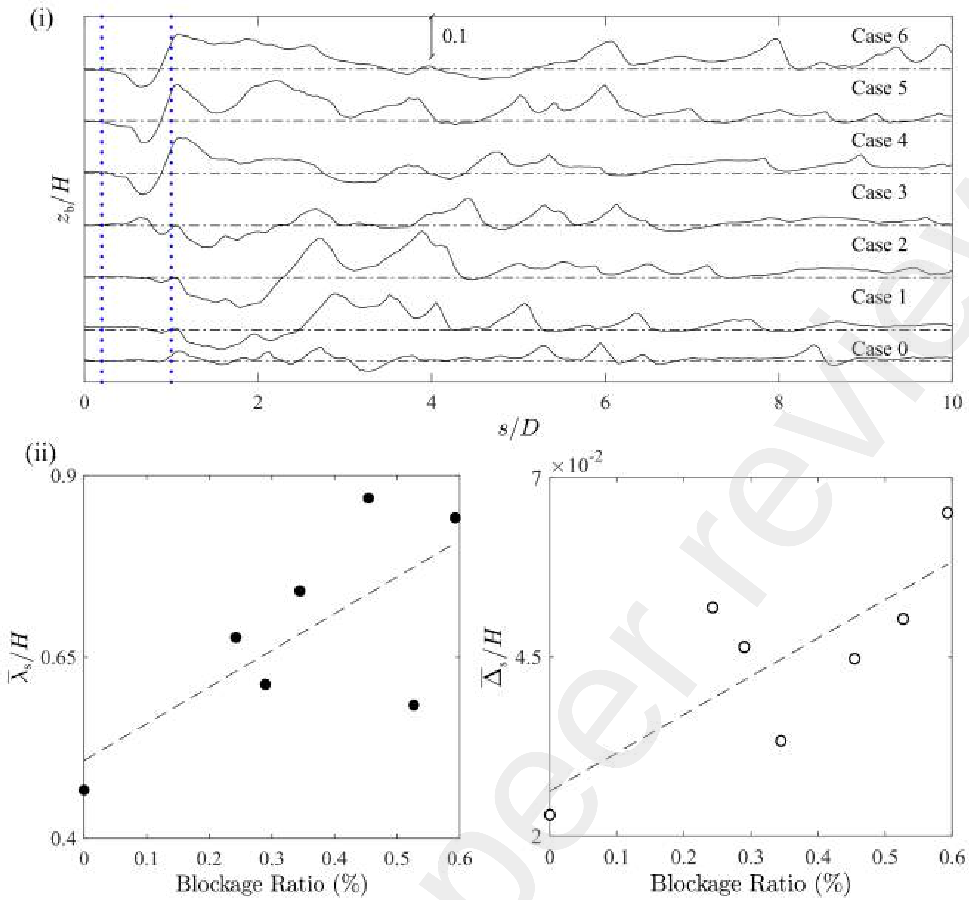

Fig. 8. LES-computed sand wave quantities at equilibrium state for cases 0 to 6. (i) depicts profiles of bed elevation along '***s***' vectors, as shown in Fig. 7. The initial part of the profiles ($x/D < 2$) corresponds to the main scour region in the turbine's wake. The horizontal dashed lines in (i) show the location of the initial flatbeds. The area between the blue dotted lines shows the region where the debris cluster and turbine are located. The vertical line shows the scale of the bed elevation normalized with the flow depth. (ii) plots the mean amplitude ($\overline{\Delta}_s$) and wavelength ($\overline{\lambda}_s$) of the major sand waves over the mobile bed of the flume, normalized with the flow depth. The bold and hollow circles in (ii) correspond with the blockage ratios of various cases and are related to the data points obtained from cases 0 to 6 for the dimensionless wavelength and amplitude of bedforms, respectively.

Moreover, by analyzing the time series of the maximum scour depth and the maximum height of the deposition zone in the turbine's wake, we attempted to quantify the two quantities for each test case (Fig. 9). The maximal values for the scour depth ($|S_d|_{\max}$) and deposition height ($|D_h|_{\max}$) were both observed in the near wake of the turbine and, in particular, beneath the turbine blades. The observed maximum scour depth and deposition height of various cases range between 0.28 m to 1.1 m and 0.5 m to 1.26 m, respectively. As seen in Fig. 9, there is a general increasing trend for both the maximum scour depth and deposition height with the blockage ratios of case 0 to 6. However, a clear deviation from this trend can be seen for case 3, which lacks the deposition sand bar seen in other debris cases. This is due to the presence of an opening within the debris cluster of case 3 that has led to a strong through-canopy jet flow, which has impeded the formation of the sand bar in the wake region.

Importantly, as shown in Fig. 7, the deposition region and the location of the maximum scour depth are not aligned with the channel's centerline. In other words, the LES computed scour patterns of the cases with debris accumulation in the turbine's wake are not symmetrical. We argue that this deviation towards the left of the wake region is due to the asymmetrical nature of the logged woody debris structure that induced an asymmetrical wake flow. This is consistent with the findings of the Yagci et al. [77]. They found that the random porosity of debris structure could lead to asymmetrical scour patterns owing to the arbitrary nature of the so-called ”bleed-flow” through the debris, which could impede the general flow and scour patterns in the wake of the tower, i.e., the von-Karman vortex streets (also see [78]). Such asymmetry is, however, absent in the scour regions of case 0 (rows 1 and 2 of Fig. 7), which has no debris accumulation. In both RANS- and LES-computed scour patterns, the dominant effect of the von Karman vortex streets is observed to induce relatively more symmetrical scour patterns.

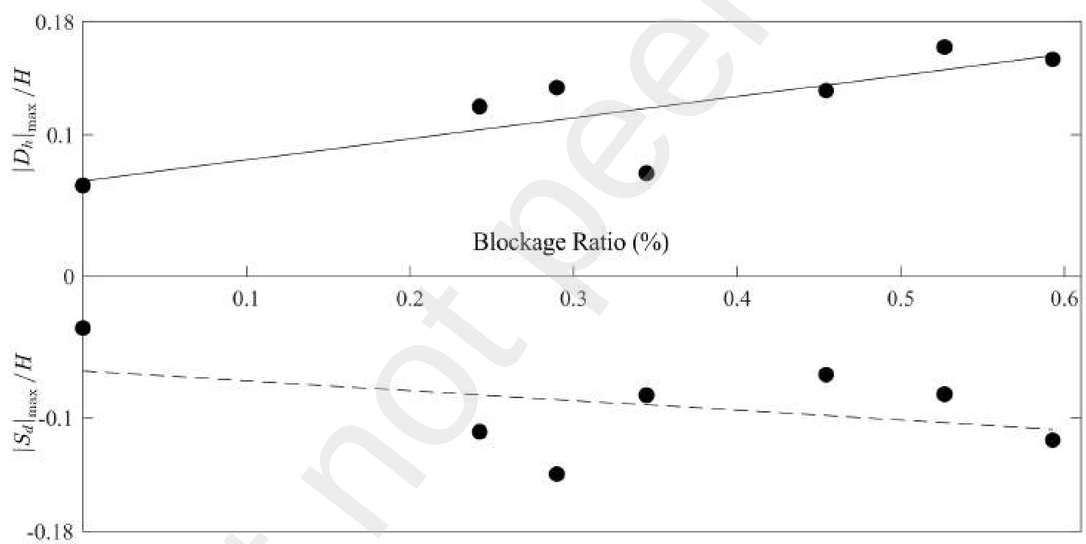

Fig. 9. Variation of the LES-computed maximum scour depth ($|S_d|_{\max}$) (dashed line) and deposition height ($|D_h|_{\max}$) (bold line) with the blockage ratios in cases 0 to 6. The maximum scour depths are in the negative bed elevation range. The two quantities are normalized with the flow depth, H. The bold circles correspond with the blockage ratios of various cases, showing the data points obtained for cases 0 to 6.

Lastly, we plot in Fig. 10 contours of dimensionless bed shear stress, i.e., Shields parameter (θ), over the deformed geometry of the bed at equilibrium state of cases 1 to 6. The Shields parameter is defined as

$$\theta = \frac{\tau_*}{(\rho_s - \rho) g d_{50}} \tag{32}$$

As seen, everywhere except for small regions below the von-Karman vortex streets, the bed shear stress is greater than the critical bed shear stress ($\theta_{cr} = 0.03$) of the sediment material. As evident in Fig. 10, such sediment hydraulics conditions have led to live bed conditions in which the bed material is ubiquitously mobilized. Based on the sediment mass balance equation (i.e., Eq.(8), the divergence of the sediment mass flux induces bed change. On the other hand, the greater the spatial variations of θ, the greater the spatial variations of sediment flux and the divergence of the sediment flux; and consequently, the bigger the bed deformation. As seen in Fig. 10, the contours of θ along the '$\boldsymbol{s}$' vector experience significant variations. The '$\boldsymbol{s}$' vector in this figure makes angles of nearly $\pm 11^o$ with the streamwise direction and originates from the turbine. This is the same path along which the major bedforms were shown to form and migrate along the same vector (see Fig. 10).

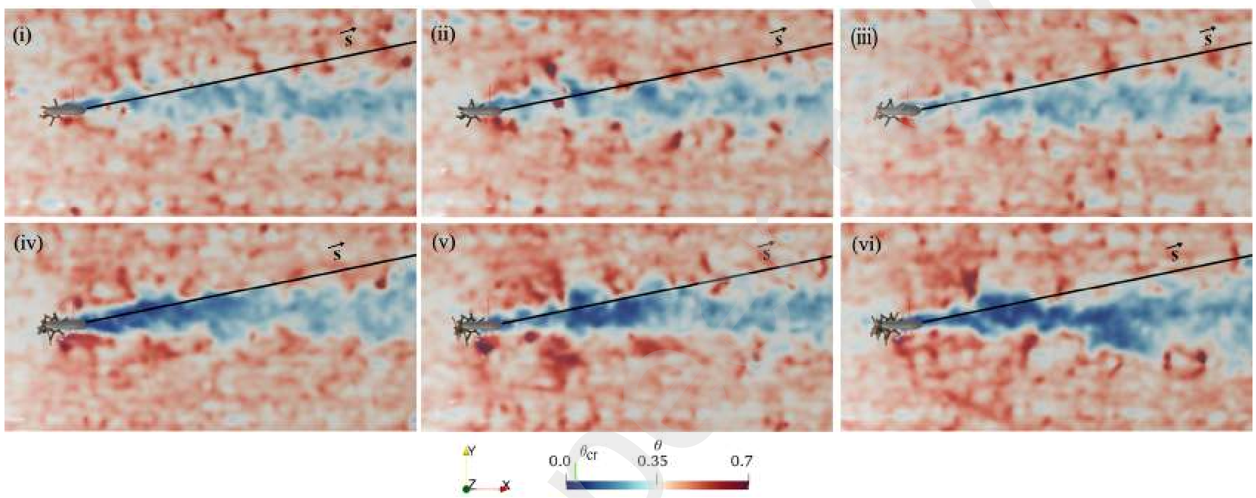

Fig. 10. Color maps of instantaneous Shields parameter, θ, projected over the deformed bed at the dynamic equilibrium state of case 1 (i), case 2 (ii), case 3 (iii), case 4 (iv), case 5 (v), and case 6 (vi). The black lines, which make angles about $\pm 11^o$ with the streamwise direction, mark the vector '$\boldsymbol{s}$' along which θ has the greatest viability and the major bedforms form and migrate (also see '$\boldsymbol{s}$' vector in Fig. 6). The green line over the legend's scale shows the value of the critical Shield parameter, i.e., $\theta_{\text{cr}} = 0.03$. Flow is from left to right.

4.3. Wake recovery

In an attempt to examine the wake momentum deficit of the turbine under the effect of woody debris and bed mobility, we utilized the first-order turbulence statistic of the wake flow field, i.e., the mean streamwise velocity. Fig. 11 plots the longitudinal profile of the mean streamwise velocity, which is averaged over the rotor's swept area. The mean streamwise velocity in the rotor's swept area is calculated as follows [59]:

$$\overline{u}_{\text{RA}} = \frac{4}{\pi D^2} \int_{A_{\text{rot}}} \overline{u}\, \mathrm{d}A \tag{33}$$

where $\overline{u}_{\text{RA}}$ denotes the mean streamwise velocity over the rotor's swept area, $\overline{u}$ is the time-averaged streamwise velocity component in the rotor's swept area, and A_{rot} is the rotor's swept area.

As seen in Fig. 11(i) for the rigid bed conditions, the mean streamwise velocities of various cases start to reduce at about $1D$ upstream of the turbine, where the debris cluster is located. The wake deficit of all cases increases until the mean streamwise velocities reach their minimum at about $0.5D$ downstream of the turbine tower. The minimum mean velocities, i.e. the maximum wake deficit, of cases 0 to 6 are $0.8727U_\infty$, $0.8515U_\infty$, $0.8483U_\infty$, $0.8418U_\infty$, $0.8277U_\infty$, $0.8070U_\infty$, and $0.7992U_\infty$, respectively. Downstream of $0.5D$, wake recovery for various cases is initiated, although it occurs at different rates. It is clear that introducing debris clusters contributes to the momentum deficit and that the denser the debris accumulation, the greater the momentum deficit. For example, comparing case 0 (i.e., the case with no debris) with case 6 (i.e., the case with the highest density of debris accumulation), it is evident that the minimum $\overline{u}_{\mathrm{RA}}$ of case 6 is about 9% less than that of case 0. Importantly, we note that the wake recovery of the cases with debris accumulation occurs at a higher rate than that of the no debris case, and at $4D$ downstream of the turbine, the mean streamwise velocities of all cases are nearly converged.

Now, we focus on the wake recovery of the cases under live bed conditions plotted in Fig. 11(ii). As seen, considering the effect of debris clusters, a trend similar to that of the rigid bed is obtained for the longitudinal profiles of the mean streamwise velocity. In other words, as the density of the debris accumulation increases, the wake deficit increases. The mean streamwise velocities reach their minimum at about $0.5D$ downstream for the turbine. Eventually, $\overline{u}_{\mathrm{RA}}$ of cases 0 to 6 converge at about $6D$ downstream of the turbine, which is $2D$ farther downstream of the convergence distance for the rigid bed condition, as seen in Fig. 11(i). We also note that the wake recovery of cases 5 and 6 under live bed conditions is slightly slower than that of the rigid bed condition.

Furthermore, the maximum wake deficits associated with the live bed condition are almost the same as those of the rigid bed. More specifically, the minimum mean streamwise velocities of cases 0 to 6 for liver bed conditions are $0.8680U_\infty$, $0.8563U_\infty$, $0.8474U_\infty$, $0.8438U_\infty$, $0.8369U_\infty$, $0.7931U_\infty$, and $0.8016U_\infty$, respectively. On average, the minimum $\overline{u}_{\mathrm{RA}}$ of the cases under live bed conditions is only 0.15% less than that of the rigid bed cases, which marks an insignificant difference between the maximum wake deficit of the two different bed conditions. In other words, based on the longitudinal variation of the first-order turbulence statistics, $\overline{u}_{\mathrm{RA}}$, the live bed condition neither impedes nor accelerates the wake recovery in a meaningful manner. This is inconsistent with the findings of Yang et al. [35] for the wake recovery under mobile bed conditions. We argue that this inconsistency can be attributed to the differences between the live bed and mobile bed conditions. More specifically, under mobile bed conditions, the bed deformations, i.e., scour and sand bar developments, are limited to a relatively small area in the wake of the turbine where the bed shear stresses are locally elevated. Thus, locally elevated bed shear stresses in a mobile bed scenario lead to solely local bed deformations. In the present study, however, we generated the live bed conditions under which the bed deformations occur throughout the flume's bed, and a wide range of sand waves are present. As a result, the bed deformation encountered in live bed conditions would modulate the wake flow quite differently than those found in mobile bed conditions.

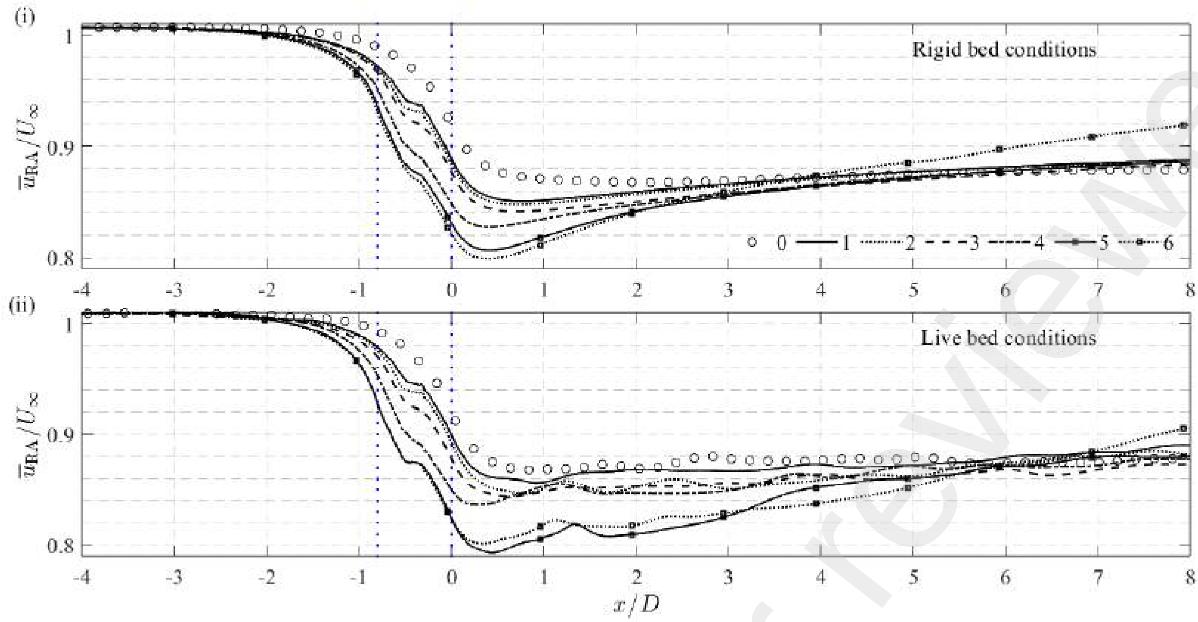

Fig. 11. Variations of normalized mean streamwise velocity averaged over the rotor swept area along the streamwise direction under (i) rigid and (ii) mobile bed conditions. Hollow circles, solid, dotted, dashed, dotted-dashed, solid with circle markers, and dotted with circle marker lines represent the results of cases 0 to 6. Blue dotted lines mark the region between the debris cluster and the turbine tower.

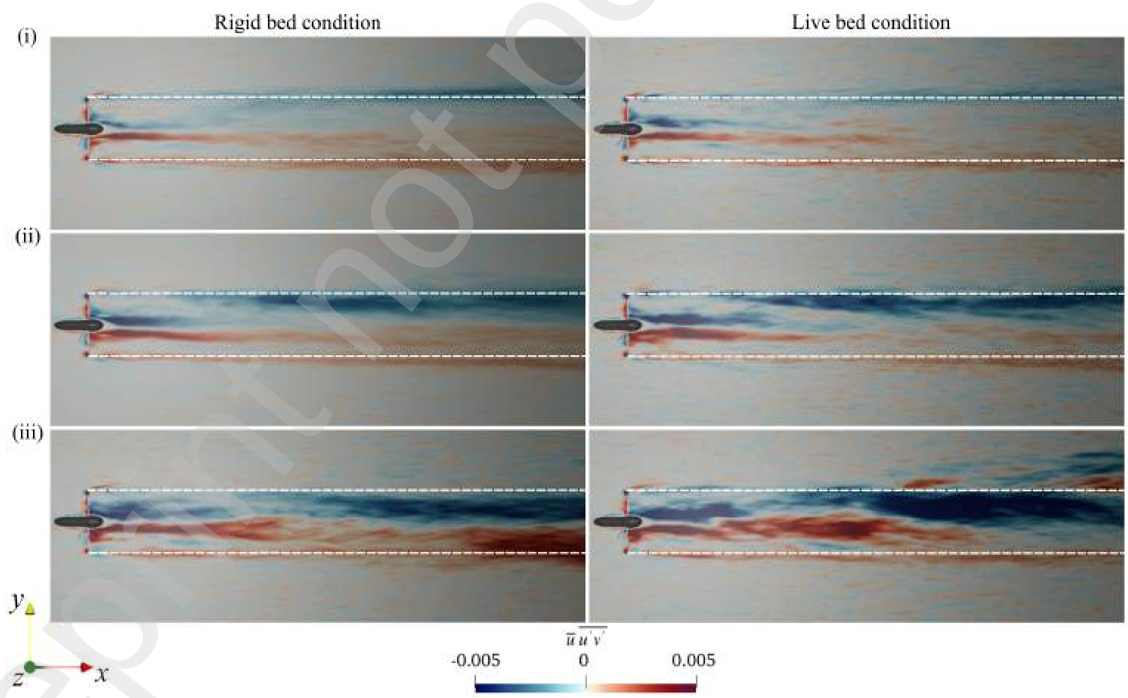

Fig. 12. Color maps of the turbulence convection term ($\overline{u}\ \overline{u'v'}$) over the horizontal planes at the rotor hub height for case 0 (i), case 3 (ii), and case 6 (iii) under the rigid and live bed conditions. Dashed white lines mark the rotor swept area region.

We examine the kinetic energy the debris cluster entrains into the wake flow to further elaborate on the wake characteristics. To do so, we introduce the mean kinetic energy transport equation as follows [79]:

$$\frac{\partial \overline{E}}{\partial t} = -\overline{u}_j \frac{\partial \overline{E}}{\partial x_j} - \frac{\partial}{\partial x_j}\left[\overline{u}_i \overline{u_i' u_j'} + \overline{u_i \tau_{ij}}\right] + \left(\overline{u_i' u_j'} + \overline{\tau_{ij}}\right)\frac{\partial \overline{u_i}}{\partial x_j} - \frac{1}{\rho}\frac{\partial (\overline{u_i}\overline{P})}{\partial x_j} + \overline{u_i}\overline{F}_i \tag{34}$$

where $\overline{E}$ $(= 1/2\overline{u_i}\overline{u_i})$ denotes mean kinetic energy. $\overline{F}_i$ is the forces exerted by the turbine and the debris accumulation. The right-hand side of Eq.(34) represents various physical modulations affecting the mean kinetic energy entrainment, in the following order: the convection by mean flow and turbulent, diffusion by the molecular and eddy viscosity, turbulent production, dissipation, transport due to mean pressure, and external forces. As highlighted in [35, 80], the turbulent convection term dominantly determines the mixing process of the flow field. Thus, we present the color maps of turbulent convection terms along the horizontal plane intersecting with the hub height of the rotor ($\overline{u}\ \overline{u'v'}$) in Fig. 12. Positive terms are colored in red, implying that the mean kinetic energy moves through the left bank of the flume, whereas negative values of the turbulence convection point out the direction of the mean kinetic energy through the right bank. Therefore, the momentum entrainment into the wake is given by the flux due to turbulence along the edges of the turbine wake denoted by the dashed white lines observed in Fig. 12. As seen in the first row of this figure, i.e., case 0 without debris, the mean kinetic energy is entrained into the wake along the tip of the blades. The flux of the mean kinetic energy, owing to the turbulence in the wake of the nacelle, is also observed at the center of the wake. This flux is the main contributor to the momentum diffusion within the wake. In cases 3 and 6, the higher blockage area of the debris cluster intensifies the momentum pick up of the wake flow (see Fig. 12(ii) and (iii)). This agrees with the observations of the rotor averaged velocity (Fig. 11), where a faster recovery of the rotor averaged velocity is observed at higher debris densities. The live bed conditions show an increase in the mixing of the mean kinetic energy in the turbine's wake. However, the energy entrainment from the outer flow into the wake is rather complex due to the flow's interaction with the bed, inducing larger variations of the kinetic energy flux in and out of the wake region than in the rigid bed cases. Its effect is also observed in the rotor averaged velocity (Fig. 11), which also presents sudden variations along the streamwise direction.

4.4. Turbine's power production

In this section, we examine the effect of woody debris accumulation on the turbine's power production under live and rigid bed conditions. To do so, we analyzed the results of different cases of computed power production. More specifically, we examined two power-related quantities: (1) the mean power coefficient of the turbine, i.e., $C_\mathrm{P} = 2\bar{P}/\rho A U_\infty^3$, where $\bar{P}$ is the computed mean power production of the turbine, and (2) the mean amplitude of the variations in the instantaneous power production of the turbine, which is defined as the difference between the maximum and minimum power production.

In Figure 13(i), we plot the variation of mean power coefficient with blockage ratios of cases 0 to 6 for both the live and rigid bed conditions. On average, the mean power coefficient of the turbine reduces from case 0 to case 6. In other words, as the blockage ratio of the debris accumulation increases, the mean power coefficient as well as the turbine's efficiency decrease. The mean power coefficient of the cases under live bed conditions is also slightly greater than that of the rigid bed conditions. This is evident in the linear representation of the live bed versus rigid bed conditions obtained using the least square method. As seen, the bold line, which represents the results of the live bed conditions, is consistently above that of the dashed line that corresponds to the rigid bed conditions. We note that the difference between the mean power coefficient of the two-bed conditions equals about 0.05.

Figure 13(ii) depicts the variations of the mean amplitude of the power fluctuation with blockage rations of cases 0 to 6 under the live and rigid bed conditions. As seen, the amplitude of power fluctuations increases with the increase of the blockage ratio [50]. Also, the amplitude of the power fluctuations under live bed conditions is significantly greater than that under rigid bed conditions. These two increasing trends of the amplitude of power fluctuations can be attributed to the effect of debris accumulation and bed deformations on the flow and turbulence kinetic energy distribution around the turbine. In other words, the greater blockage ratio and density of the debris accumulation leads to larger flow structures that pass by the turbine, inducing greater variations in power production. The bed deformations and sand waves could also lead to more fluctuations in the flow, and power production by consequence.

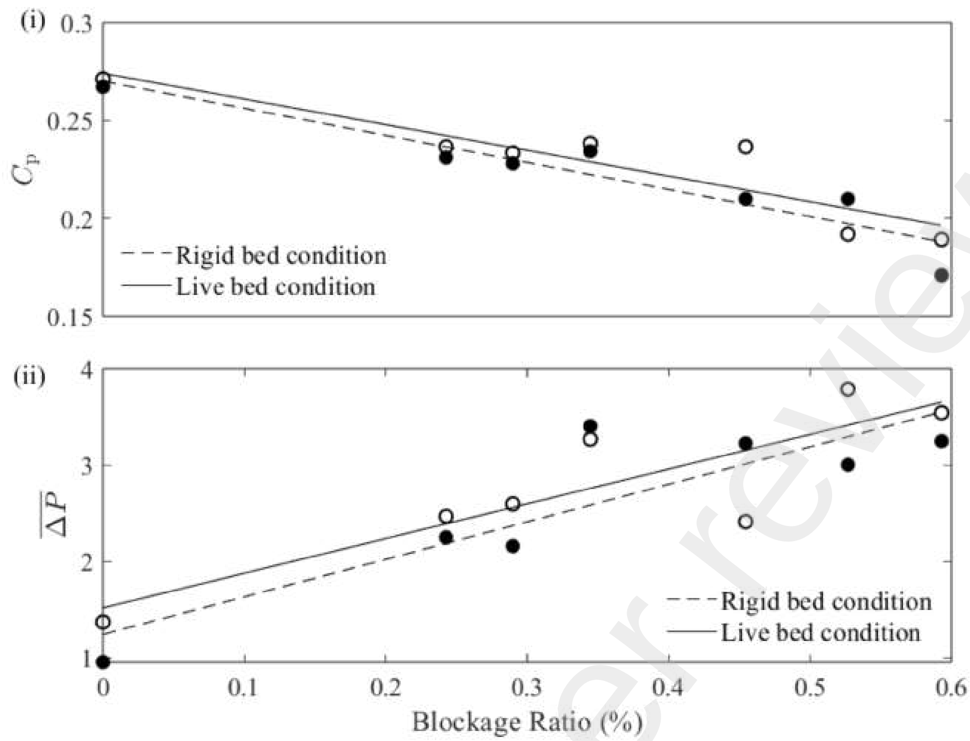

Fig. 13. Computed mean power coefficient (i) and mean power variation amplitude (ii) for various debris buildups in terms of the percentage of blockage ratio under rigid and live bed conditions. The bold and hollow circles correspond with the blockage ratios of various cases, showing the data points obtained for cases 0 to 6 for rigid and live bed conditions, respectively.

5. Conclusion

We performed a series of LES coupled with a morphodynamics model to evaluate the effect of different woody debris' blockage ratios on the wake flow and power production of a utility-scale turbine under both rigid and live bed conditions. The turbine blades were parameterized using the actuator line model, while the turbine's nacelle was represented using the actuator surface model. The turbine tower and individual woody logs were simulated using their detailed geometry. Further, the bed morphodynamics model solves the sediment mass balance equation and corrects the bed surface using a mass-balanced sand slide model to ensure the bed surface angles are limited to the angle of repose of the bed sediment material.

Our simulation results under the rigid bed conditions revealed that the gradual increase of debris accumulation over the turbine tower augments the spanwise size and intensity of the momentum deficit in the wake of the turbine. Further analysis of the mean flow statistics showed that, owing to gaps between logs, several intense through-canopy jet flows occur, which increase the turbulence kinetic energy of the wake flow, contributing to the wake recovery of the turbine. Overall, these numerical observations showed that the increasing accumulation of woody debris significantly modulates the wake deficit of the turbine and, consequently, the turbine's power production.

Our simulation results in the live bed conditions revealed a complex interaction between the mobile bed and the turbulent flow through the debris cluster, leading to asymmetrical turbulence and kinetic energy distribution. Owing to such interactions, the wake flow of various cases in the lower flow depth is associated with equally high turbulence kinetic energy, and the debris density variations seem less important than the rigid bed conditions. Further, our simulations under the live bed conditions captured the initiation, growth, and migration of sand waves in all cases of debris accumulation. The most dominant sand waves were observed in the turbine's wake and propagated downstream along two main vectors with angles of 11° relative to the streamwise direction. The two lines were shown to overlap with the edges of the wake region in the spanwise direction, where the shear layer is strong. Moreover, it was shown that the sand waves' wavelength and amplitude increased from cases 0 to 6, marking the impact of debris accumulation on the evolving bed deformations. A similar trend was also discovered for the maximum depth of the scour hole and deposition sand bar in the turbine's wake. In other words, as we increased the blockage ratio of the debris cluster, the scour hole in the turbine's wake became deeper.

Our wake recovery analysis based on the mean streamwise velocity over the rotor swept area showed that the debris accumulations with higher blockage ratios lead to a greater wake deficit at about $0.5D$ downstream of the turbine. Farther downstream, the wave recovery of cases 1 to 6 is relatively rapid. As a result, the mean streamwise velocity over the rotor area of various debris cases reaches that of the no debris case at about $4D$ and $6D$ under the rigid and live bed conditions, respectively. We also analyzed the wake recovery of the turbine using the plots of the mean kinetic energy flux due to turbulence. This analysis showed that the high density of debris accumulation intensifies the entrainment of the momentum into the wake region, accelerating the wake recovery of the turbine.

Importantly, we investigated the debris accumulation effect on the turbine's power production under rigid and live bed conditions. We observed that for both bed conditions, on average, the turbine's power production reduces as the debris clusters' blockage area increases. In other words, debris clusters reduce the efficiency of the turbine, which is proportional to the density of the debris clusters. Moreover, it was observed that the amplitude of the variations in power production increases with the density of the debris cluster. Regarding the effect of live bed conditions and bed deformations on the turbine efficiency, it was observed that the power production under live bed conditions is slightly greater than that under rigid bed conditions.

Finally, we will use the lessons learned in this work to conduct LES of virtually installed arrays of MHK turbines in a real-life setting at the University of New Hampshire's tidal energy test site. This test site is located at the General Sullivan Bridge with a tidal range of about 2.5 m, resulting in a peak flow velocity of more than 2 m/s.

6. Acknowledgements

This work was supported by grants from the U.S. Department of Energy's Office of Energy Efficiency and Renewable Energy (EERE) under the Water Power Technologies Office (WPTO) Award Number DE-EE0009450 and NSF (grant number 2233986). The views expressed herein do not necessarily represent the view of the U.S. Department of Energy or the United States Government. The Civil Engineering Department, Stony Brook Research Computing and Cyber Infrastructure, and the Institute for Advanced Computational Science at Stony Brook University provided the computational resources.

7. Data Availability Statement

The code for the numerical model, including the actuator line model (10.5281/zenodo.10521565), simulation results for the flow field (10.5281/zenodo.10521509), power production of the test cases (10.5281/zenodo.10521545),and instantaneous bed morphology at equilibrium conditions for all cases under live bed conditions (10.5281/zenodo.10967316) are made available in the online repository of Zenodo.

Appendix A. Validation study

Herein, we present a validation study to examine the LES results of the model against the experimental data of Kang et al. [75], who measured the wake flow field of two longitudinally aligned laboratory-scale horizontal-axis tidal turbines. The two models of MHK turbines had a rotor diameter of 0.16 m and were installed in a 0.9 m wide and 0.37 m depth channel.

We employed a non-uniform computational grid system, which was refined to have a resolution of 0.8 mm in all directions around the turbine blades. Outside of the rotor area, the grid system was stretched to reach its lowest resolution of 24 mm, 7 mm, and 8 mm in the streamwise, spanwise, and vertical directions, respectively, resulting in a total of 142 million grid nodes. Additionally, the simulation used a dimensional time step of 0.011 seconds to maintain a Courant-Friedrichs-Lewy (CFL) number less than 1 (Table A.4).

The incoming velocity (U_∞) was set equal to 0.19 m/s for a Reynolds number of 3.5×10^4. The distance between the two turbines was 0.8 m, and the two turbines' tip-speed ratio (λ) was 5.1. The wall model (presented in Section 2) was employed to reconstruct the near-wall velocity field. A separate precursor simulation was used to generate the turbulent inflow conditions of the main LES.

Table A.4: Details of the computational grid system and time step of flow solver in the validation study. N_x, N_y, and N_z are the number of computational grid nodes in the streamwise, spanwise, and vertical directions, respectively. Δx_{d}, Δy_{d}, and Δz_{d} are spatial steps of the flow solver in the rotor area, while $\Delta x_{\max}$, $\Delta y_{\max}$, and $\Delta z_{\max}$ are the coarsest spatial steps outside the rotor area in the streamwise, spanwise, and vertical directions, respectively. Δz^+ is the grid spacing in the vertical direction scaled by inner wall units near the blades. Δt is the flow solver's time step.

Variable	Grid
N_x, N_y, N_z	$869 \times 521 \times 317$
Δx_{d}, Δy_{d}, Δz_{d} (mm)	0.8
$\Delta x_{\max}$, $\Delta y_{\max}$, $\Delta z_{\max}$ (mm)	24, 7, 8
Δz^+	70
Δt (s)	0.011

In Fig. A.14, we compare the LES computed results of the mean velocity deficit and turbulence kinetic energy with the measured data along the streamwise direction. This comparison includes the near field of the first turbine and the near and far fields of the second turbine, as detailed in Kang et al. [75]. In the wake of the first turbine, the LES model slightly overestimated the velocity deficit while it captured the turbulence kinetic energy with good accuracy. In the wake of the second turbine, however, the LES computations slightly overestimate the turbulence kinetic energy while the velocity deficit is captured quite well. The near-field predictions of the LES for both quantities, in the wake of the second turbine, are higher than the measurements, while the far-field predictions of the LES are in better agreement with the measurements. This tendency can be attributed to the near and far field computations of the actuator line model, which is shown to perform better in the far field than the near field [31, 32, 51, 56]. Overall, there is a reasonable agreement between the LES computations and the experimental data.

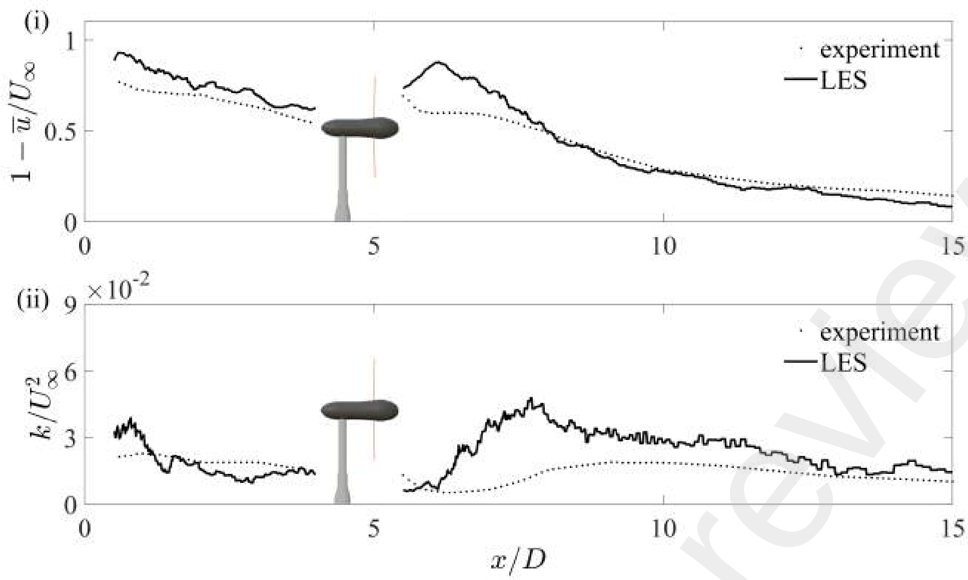

Fig. A.14. LES-computed (bold line) and measured (dotted line) [75] longitudinal profiles of the velocity deficit (i) and turbulence kinetic energy (ii). The profiles start from $0.5D$ downstream of the first turbine to $10D$ downstream of the second turbine in the streamwise direction at the hub height (z = 0.85D). The parameters are normalized by the incoming velocity (U_∞ = 0.19 m/s) at the hub height.

Appendix B. Grid sensitivity analysis

Herein, we report a grid independence analysis to investigate the grid dependence of the LES results for case 3 under the rigid bed conditions. We employed three successively refined spatial resolutions with details presented in Table B.5. The three grid systems are denoted as grids A, B, and C, leading to 9 to 40 million computational grid nodes.

In Fig. B.15, we compare $\overline{u}_{\mathrm{RA}}$ (i.e., the mean streamwise velocity averaged over the swept area of the rotor) of case 3 obtained from grids A, B, and C under the rigid bed conditions. This comparison was intended to find a suitable grid resolution with the lowest computational cost. While the computed $\overline{u}_{\mathrm{RA}}$ varies considerably between grids A and B, it aligns fairly well between grids B and C, especially in the near field region. Grid B achieves a resolution comparable to grid C without the same level of refinement, and thus it was selected to perform this study's simulations.

Table B.5: Details of the computational grid systems A, B, and C and their corresponding time steps. N_x, N_y, and N_z are the number of computational grid nodes in the streamwise, spanwise, and vertical directions, respectively. Δx, Δy, and Δz are spatial steps of the flow solver normalized with the rotor diameter, D. $\Delta t = t(U_\infty/D)$ is the flow solver's non-dimensional time step, where t is the dimensional time step. Δz^+ is the minimum grid spacing in the vertical direction scaled by inner wall units.

Variable	Grid A	Grid B	Grid C
Number of grid nodes	9×10^6	19×10^6	40×10^6
N_x, N_y, N_z	$209 \times 68 \times 585$	$253 \times 81 \times 881$	$349 \times 109 \times 1025$
$\Delta x, \Delta y, \Delta z$	0.025	0.02	0.015
Δt	0.001	0.001	0.001
Δz^+	1400	1000	800

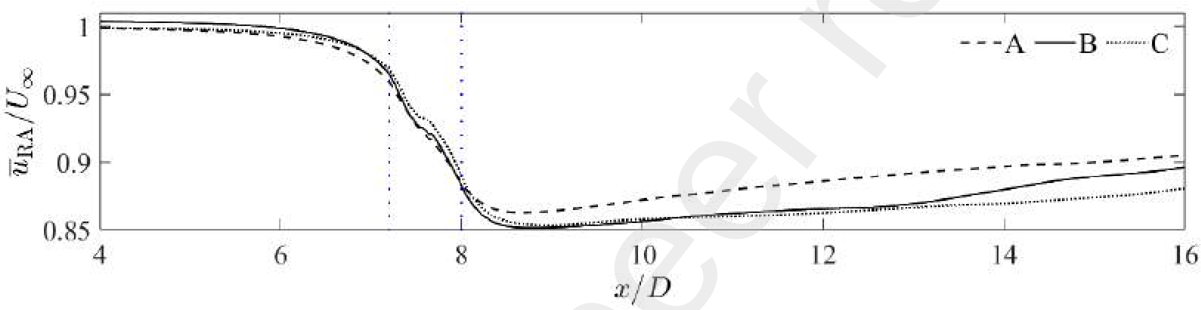

Fig. B.15. Variations of the LES-computed mean streamwise velocity averaged over the rotor swept area, $\overline{u}_{\mathrm{RA}}$, for the case 3 using grids A (dashed line), B (bold line), and C (dotted line) under the rigid bed conditions. The velocity is normalized with U_∞. Blue dotted lines are drawn respectively at $7.2D$ and $8D$ to indicate the upstream face of the debris cluster and the turbine tower.

References

[1] A. Hussain, S. M. Arif, M. Aslam, Emerging renewable and sustainable energy technologies: State of the art, Renewable and Sustainable Energy Reviews 71 (2017) 12–28. doi:http://dx.doi.org/10.1016/j.rser.2016.12.033.

[2] Global Energy Review 2021, Technical Report, International Energy Agency, 2021. URL: https://www.iea.org/reports/global-energy-review-2021/renewables.

[3] L. Kilcher, M. Fogarty, M. Lawson, Marine Energy in the United States: An Overview of Opportunities, Technical Report, National Renewable Energy Laboratory, 2021. URL: https://www.nrel.gov/docs/fy21osti/78773.pdf.

[4] Quadrennial Technology Review 2015, Technical Report, United States Department of Energy, 2015. URL: https://www.energy.gov/quadrennial-technology-review-2015.

[5] Renewables 2016: Global Status Report, Technical Report, Renewable Energy Policy Network for the 21st Century, 2016. URL: https://www.ren21.net/gsr-2016/.

[6] M. Nachtane, M.Tarfaoui, I. Goda, M. Rouway, A review on the technologies, design considerations and numerical models of tidal current turbines, Renewable Energy 157 (2020) 1274–1288. doi:https://doi.org/10.1016/j.renene.2020.04.155.

[7] A. Khosronejad, J. L. Kozarek, F. Sotiropoulos, Simulation-based approach for stream restoration structure design: Model development and validation, Journal of Hydraulic Engineering 140 (2014) 04014042. doi:10.1061/(ASCE)HY.1943-7900.0000904.

[8] A. Khosronejad, F. Sotiropoulos, On the genesis and evolution of barchan dunes: morphodynamics, Journal of Fluid Mechanics 815 (2017) 117–148. doi:10.1017/jfm.2016.880.

[9] A. Khosronejad, S. Kang, I. Borazjani, F. Sotiropoulos, Curvilinear immersed boundary method for simulating coupled flow and bed morphodynamic interactions due to sediment transport phenomena, Advances in Water Resources 34 (2011) 829–843. doi:https://doi.org/10.1016/j.advwatres.2011.02.017.

[10] A. Khosronejad, F. Sotiropoulos, Numerical simulation of sand waves in a turbulent open channel flow, Journal of Fluid Mechanics 753 (2014) 150–216. doi:10.1017/jfm.2014.335.

[11] A. Khosronejad, J. L. Kozarek, P. Diplas, C. Hill, R. Jha, P. Chatanantavet, N. Heydari, F. Sotiropoulos, Simulation-based optimization of in-stream structures design: rock vanes, Environmental Fluid Mechanics 18 (2018) 695–738. doi:10.1007/s10652-018-9579-7.

[12] A. Khosronejad, A. B. Limaye, Z. Zhang, S. Kang, X. Yang, F. Sotiropoulos, On the morphodynamics of a wide class of large-scale meandering rivers: Insights gained by coupling les with sediment-dynamics, Journal of Advances in Modeling Earth Systems 15 (2023). doi:https://doi.org/10.1029/2022MS003257.

[13] C. Camporeale, P. Perona, A. Porporato, L. Ridolfi, Hierarchy of models for meandering rivers and related morphodynamic processes, Reviews of Geophysics 45 (2007). doi:https://doi.org/10.1029/2005RG000185.

[14] T. Stoesser, Large-eddy simulation in hydraulics: Quo vadis?, Journal of Hydraulic Research 52 (2014) 441–452. doi:10.1080/00221686.2014.944227.

[15] U. S. W. P. T. Office, Tidal testing underway in New York's East River, https://www.energy.gov/eere/water/articles/tidal-testing-underway-new-yorks-east-river, 2021.

[16] N. D. Laws, B. P. Epps, Hydrokinetic energy conversion: Technology, research, and outlook, Renewable and Sustainable Energy Reviews 57 (2016) 1245–1259. doi:http://dx.doi.org/10.1016/j.rser.2015.12.189.

[17] T. Engineering, Fundy ocean research center for energy (force) test site, https://tethys.pnnl.gov/project-sites/fundy-ocean-research-center-energy-force-test-site, 2024.

[18] T. Engineering, Meygen tidal energy project, https://tethys.pnnl.gov/project-sites/meygen-tidal-energy-project, 2024.

[19] S. G. Jérôme Thiébot, Pascal Bailly du Bois, Numerical modeling of the effect of tidal stream turbines on the hydrodynamics and the sediment transport e application to the alderney race (raz blanchard), france, Renewable Energy 75 (2015) 356–365. doi:https://doi.org/10.1016/j.renene.2014.10.021.

[20] C. Sun, W. H. Lam, M. Dai, G. Hamill, Prediction of seabed scour induced by full-scale darrieus-type tidal current turbine, Journal of Marine Science Engineering 7 (2017). doi:https://doi.org/10.3390/jmse7100342.

[21] Renewables 2016: Global Status Report, Technical Report, Office of Energy Efficiency and Renewable Energy, 2022. URL: https://www.energy.gov/eere/analysis/renewable-energy-resource-assessment-information-united-states.

[22] M. Musa, C. Hill, M. Guala, Interaction between hydrokinetic turbine wakes and sediment dynamics: array performance and geomorphic effects under different siting strategies and sediment transport conditions, Renewable Energy 138 (2019) 738–753. doi:https://doi.org/10.1016/j.renene.2019.02.009.

[23] S. Chawdhary, D. Angelidis, J. Colby, D. Corren, L. Shen, F. Sotiropoulos, Multiresolution large-eddy simulation of an array of hydrokinetic turbines in a field-scale river: The roosevelt island tidal energy project in new york city, Water Resources Research 54 (2018) 10188–10204. doi:https://doi.org/10.1029/2018WR023345.

[24] C. Hill, M. Musa, M. Guala, Interaction between instream axial flow hydrokinetic turbines and uni-directional flow bedforms, Renewable Energy 86 (2016) 409–421. doi:https://doi.org/10.1016/j.renene.2015.08.019.

[25] C. Hill, J. Kozarek, F. Sotiropoulos, M. Guala, Hydrodynamics and sediment transport in a meandering channel with a model axial-flow hydrokinetic turbine, Water Resources Research (2016) 860–879. doi:https://doi.org/10.1002/2015WR017949.

[26] M. Musa, C. Hill, F. Sotiropoulos, M. Guala, Performance and resilience of hydrokinetic turbine arrays under large migrating fluvial bedforms, Nature Energy 3 (2018) 839–846. URL: https://doi.org/10.1038/s41560-018-0218-9. doi:10.1038/s41560-018-0218-9.

[27] X. Lin, J. Zhang, R. Wang, J. Zhang, W. Liu, Y. Zhang, Scour around a mono-pile foundation of a horizontal axis tidal stream turbine under steady current, Ocean Engineering 192 (2019) 106571. doi:10.1016/j.oceaneng.2019.106571.

[28] L. Chen, R. Hashim, F. Othman, S. Motamedi, Experimental study on scour profile of pile-supported horizontal axis tidal current turbine, Renewable Energy 114 (2017) 744–754. doi:https://doi.org/10.1016/j.renene.2017.07.026.

[29] R. Ramírez-Mendoza, L. Amoudry, P. Thorne, R. Cooke, S. McLelland, L. Jordan, S. Simmons, D. Parsons, L. Murdoch, Laboratory study on the effects of hydro kinetic turbines on hydrodynamics and sediment dynamics, Renewable Energy 129 (2018) 271–284. doi:https://doi.org/10.1016/j.renene.2018.05.094.

[30] J. Jeon, Y. Kim, D. Kim, S. Kang, Flume experiments for flow around debris accumulation at a bridge, KSCE Journal of Civil Engineering (2024) 1–13. doi:doi.org/10.1007/s12205-024-1442-4.

[31] P. O. Peter K. Stansby, Modelling marine turbine arrays in tidal flows, Journal of Hydraulic Research 60 (2022) 187–204. doi:https://doi.org/10.1080/00221686.2021.2022032.

[32] S. Kang, X. Yang, F. Sotiropoulos, On the onset of wake meandering for an axial flow turbine in a turbulent open channel flow, Journal of Fluid Mechanics 744 (2014) 376–403. doi:doi:10.1017/jfm.2014.82.

[33] C. Liu, C. Hu, An actuator line - immersed boundary method for simulation of multiple tidal turbines, Renewable Energy 136 (2019) 473–490. doi:https://doi.org/10.1016/j.renene.2019.01.019.

[34] M. Musa, M. Heisel, M. Guala, Predictive model for local scour downstream of hydrokinetic turbines in erodible channels, Phys. Rev. Fluids 3 (2018) 024606. doi:10.1103/PhysRevFluids.3.024606.

[35] X. Yang, A. Khosronejad, F. Sotiropoulos, Large-eddy simulation of a hydrokinetic turbine mounted on an erodible bed, Renewable Energy 113 (2017) 1419–1433. doi:https://doi.org/10.1016/j.renene.2017.07.007.

[36] R. Ramirez-Mendoza, L. Murdoch, L. Jordan, L. Amoudry, S. McLelland, R. Cooke, P. Thorne, S. Simmons, D. Parsons, M. Vezza, Asymmetric effects of a modelled tidal turbine on the flow and seabed, Renewable Energy 159 (2020) 238–249. doi:https://doi.org/10.1016/j.renene.2020.05.133.

[37] X. Deng, J. Zhang, X. Lin, Proposal of actuator line-immersed boundary coupling model for tidal stream turbine modeling with hydrodynamics upon scouring morphology, Energy 292 (2024) 130451. doi:https://doi.org/10.1016/j.energy.2024.130451.

[38] E. Wohl, D. N. Scott, Wood and sediment storage and dynamics in river corridors, Earth Surface Processes and Landforms 42 (2017) 5–23. doi:https://doi.org/10.1002/esp.3909.

[39] H. Ghaffarian, P. Lemaire, Z. Zhi, L. Tougne, B. MacVicar, H. Piégay, Automated quantification of floating wood pieces in rivers from video monitoring: a new software tool and validation, Earth Surface Dynamics 9 (2021) 519–537. doi:10.5194/esurf-9-519-2021.

[40] A. M. Gurnell, H. Piégay, F. J. Swanson, S. V. Gregory, Large wood and fluvial processes, Freshwater Biology 47 (2002) 601–619. doi:https://doi.org/10.1046/j.1365-2427.2002.00916.x.

[41] H. Friedrich, D. Ravazzolo, V. Ruiz-Villanueva, I. Schalko, G. Spreitzer, J. Tunnicliffe, V. Weitbracht, Physical modelling of large wood (lw) processes relevant for river management: Perspectives from new zealand and switzerland, Earth Surface Processes and Landforms 47 (2021) 32–57. doi:https://doi.org/10.1002/esp.5181.

[42] I. Schalko, L. Schmocker, V. Weitbrecht, R. M. Boes, Backwater rise due to large wood accumulations, Journal of Hydraulic Engineering 144 (2018) 04018056. doi:10.1061/(ASCE)HY.1943-7900.0001501.

[43] T. Euler, J. Zemke, S. Rodrigues, J. Herget, Influence of inclination and permeability of solitary woody riparian plants on local hydraulic and sedimentary processes, Hydrological Processes 28 (2014) 1358–1371. doi:https://doi.org/10.1002/hyp.9655.

[44] D. Panici, P. Kripakaran, Characterizing the importance of porosity of large woody debris accumulations at single bridge piers on localized scour, Water Resources Research 59 (2023). doi:https://doi.org/10.1029/2022WR033531.

[45] I. Schalko, E. Wohl, H. M. Nepf, Flow and wake characteristics associated with large wood to inform river restoration, Scientific Reports 11 (2021). doi:10.1038/s41598-021-87892-7.

[46] I. Schalko, M. Ponce, S. Lassar, S. Schwindt, S. Haun, H. Nepf, Flow and turbulence due to wood contribute to declogging of gravel bed, Geophysical Research Letters 51 (2024). doi:https://doi.org/10.1029/2023GL107507.

[47] B. D. Collins, D. R. Montgomery, K. L. Fetherston, T. B. Abbe, The floodplain large-wood cycle hypothesis: A mechanism for the physical and biotic structuring of temperate forested alluvial valleys in the north pacific coastal ecoregion, Geomorphology 139-140 (2012) 460–470. doi:https://doi.org/10.1016/j.geomorph.2011.11.011.

[48] I. Schalko, C. Lageder, L. Schmocker, V. Weitbrecht, R. M. Boes, Laboratory flume experiments on the formation of spanwise large wood accumulations: Part ii—effect on local scour, Water Resources Research 55 (2019) 4871–4885. doi:https://doi.org/10.1029/2019WR024789.

[49] I. Schalko, C. Lageder, L. Schmocker, V. Weitbrecht, R. Boes, Laboratory flume experiments on the formation of spanwise large wood accumulations: I. effect on backwater rise, Water Resources Research 55 (2019) 4854–4870. doi:https://doi.org/10.1029/2018WR024649.

[50] M. M. Aksen, K. Flora, H. Seyedzadeh, M. G. Anjiraki, A. Khosronejad, On the impact of debris accumulation on power production of marine hydrokinetic turbines: Insights gained via les, Theoretical and Applied Mechanics Letters (2024) 100524. doi:https://doi.org/10.1016/j.taml.2024.100524.

[51] Y. Zhang, E. Fernandez-Rodriguez, J. Zheng, Y. Zheng, J. Zhang, H. Gu, W. Zang, X. Lin, A review on numerical development of tidal stream turbine performance and wake prediction, IEEE Access 8 (2020) 79325–79337. doi:https://doi.org/10.1029/2018WR023345.

[52] L. Tian, Y. Song, N. Zhao, W. Shen, C. Zhu, T. Wang, Effects of turbulence modelling in ad/rans simulations of single wind & tidal turbine wakes and double wake interactions, Energy 208 (2020) 118440. doi:https://doi.org/10.1016/j.energy.2020.118440.

[53] M. H. Baba-Ahmadi, P. Dong, Validation of the actuator line method for simulating flow through a horizontal axis tidal stream turbine by comparison with measurements, Renewable Energy 113 (2017). doi:https://doi.org/10.1016/j.renene.2017.05.060.

[54] J. N. Sørensen, W. Z. Shen, Numerical modeling of wind turbine wakes, Journal of Fluids Engineering 124 (2002) 393–399. doi:https://doi.org/10.1115/1.1471361.

[55] X. Yang, F. Sotiropoulos, A new class of actuator surface models for wind turbines, Wind Energy 21 (2018) 285–302. doi:https://doi.org/10.1002/we.2162.

[56] D. D. Apsley, T. Stallard, P. K. Stansby, Actuator-line cfd modelling of tidal-stream turbines in arrays, Journal of Ocean Engineering and Marine Energy 4 (2018) 259–271. doi:https://doi.org/10.1007/s40722-018-0120-3.

[57] M. Shives, C. Crawford, Adapted two-equation turbulence closures for actuator disk rans simulations of wind & tidal turbine wakes, Renewable Energy 92 (2016) 273–292. doi:https://doi.org/10.1016/j.renene.2016.02.026.

[58] Z. Gao, Y. Li, T. Wang, W. Shen, X. Zheng, S. Pröbsting, D. Li, R. Li, Modelling the nacelle wake of a horizontal-axis wind turbine under different yaw conditions, Renewable Energy 172 (2021) 263–275. doi:https://doi.org/10.1016/j.renene.2021.02.140.

[59] C. Santoni, F. Sotiropoulos, A. Khosronejad, A comparative analysis of actuator-based turbine structure parametrizations for high-fidelity modeling of utility-scale wind turbines under neutral atmospheric conditions, Energies 17 (2024). doi:https://doi.org/10.3390/en17030753.

[60] A. Arabgolarcheh, D. Micallef, A. Rezaeiha, E. Benini, Modelling of two tandem floating offshore wind turbines using an actuator line model, Renewable Energy 216 (2023). doi:https://doi.org/10.1016/j.renene.2023.119067.

[61] E. B. Alireza Arabgolarcheh, Sahar Jannesarahmadi, Modeling of near wake characteristics in floating offshore wind turbines using an actuator line method, Renewable Energy 185 (2022) 871–887. doi:https://doi.org/10.1016/j.renene.2021.12.099.

[62] A. Posa, R. Broglia, Analysis of the momentum recovery in the wake of aligned axial-flow hydrokinetic turbines, Physics of Fluids 34 (2022). doi:https://doi.org/10.1063/5.0117882.

[63] K. Flora, A. Khosronejad, Uncertainty quantification of bank vegetation impacts on the flood flow field in the american river, california, using large-eddy simulations, Earth Surface Processes and Landforms 49 (2024) 967–979. doi:https://doi.org/10.1002/esp.5745.

[64] S. Kang, A. Lightbody, C. Hill, F. Sotiropoulos, High-resolution numerical simulation of turbulence in natural waterways, Advances in Water Resources 34 (2011) 98–113. doi:https://doi.org/10.1016/j.advwatres.2010.09.018.

[65] J. Smagorinsky, General circulation experiments with the primitive equations: I. the basic experiment, Monthly Weather Review 91 (1963) 99 – 164. doi:10.1175/1520-0493(1963)091<0099:GCEWTP>2.3.CO;2.

[66] M. Germano, U. Piomelli, P. Moin, W. H. Cabot, A dynamic subgrid-scale eddy viscosity model, Physics of Fluids A: Fluid Dynamics 3 (1991) 1760–1765. doi:10.1063/1.857955.

[67] D. C. Wilcox, Simulation of transition with a two-equation turbulence model, AIAA Journal 32 (1994) 247–255. doi:10.2514/3.59994.

[68] C. Paola, V. R. Voller, A generalized exner equation for sediment mass balance, Journal of Geophysical Research: Earth Surface 110 (2005). doi:https://doi.org/10.1029/2004JF000274.

[69] L. C. Van Rijn, Principles of sediment transport in rivers, estuaries, and coastal seas, Aqua Publications, 1993.

[70] Y. Jia, Y. Xu, S. Wang, Numerical simulation of local scouring around a cylindrical pier, in: Proceedings of ICSF-1, 1st international conference on scour of foundations, Texas A&M University, Texas, 2002.

[71] A. Khosronejad, S. Kang, F. Sotiropoulos, Experimental and computational investigation of local scour around bridge piers, Advances in Water Resources 37 (2012) 73–85. doi:https://doi.org/10.1016/j.advwatres.2011.09.013.

[72] X. Yang, F. Sotiropoulos, R. J. Conzemius, J. N. Wachtler, M. B. Strong, Large-eddy simulation of turbulent flow past wind turbines/farms: the virtual wind simulator (vwis), Wind Energy 18 (2015) 2025–2045. doi:https://doi.org/10.1002/we.1802.

[73] X. Yang, X. Zhang, Z. Li, G.-W. He, A smoothing technique for discrete delta functions with application to immersed boundary method in moving boundary simulations, Journal of Computational Physics 228 (2009) 7821–7836. doi:https://doi.org/10.1016/j.jcp.2009.07.023.

[74] K. Flora, C. Santoni, A. Khosronejad, Numerical study on the effect of bank vegetation on the hydrodynamics of the american river under flood conditions, Journal of Hydraulic Engineering 147 (2021). doi:https://doi.org/10.1061/(ASCE)HY.1943-7900.0001912.

[75] S. Kang, Y. Kim, J. Lee, A. Khosronejad, X. Yang, Wake interactions of two horizontal axis tidal turbines in tandem, Ocean Engineering 254 (2022) 111331. doi:https://doi.org/10.1016/j.oceaneng.2022.111331.

[76] L. C. van Rijn, Sediment transport, part iii: Bed forms and alluvial roughness, Journal of Hydraulic Engineering 110 (1984) 1733–1754. doi:10.1061/(ASCE)0733-9429(1984)110:12(1733).

[77] O. Yagci, M. F. Celik, V. Kitsikoudis, V. Ozgur Kirca, C. Hodoglu, M. Valyrakis, Z. Duran, S. Kaya, Scour patterns around isolated vegetation elements, Advances in Water Resources 97 (2016) 251–265. doi:https://doi.org/10.1016/j.advwatres.2016.10.002.

[78] L. Zong, H. Nepf, Vortex development behind a finite porous obstruction in a channel, Journal of Fluid Mechanics 691 (2012) 368–391. doi:10.1017/jfm.2011.479.

[79] C. Santoni, K. Carrasquillo, I. Arenas-Navarro, S. Leonardi, Effect of tower and nacelle on the flow past a wind turbine, Wind Energy 20 (2017) 1927–1939. doi:https://doi.org/10.1002/we.2130.

[80] X. Yang, K. Howard, M. Guala, F. Sotiropoulos, Effects of a three-dimensional hill on the wake characteristics of a model wind turbine, Physics of Fluids 27 (2015). doi:10.1063/1.4907685.